Journal of Luminescence 207 (2019) 1–13

Contents lists available at ScienceDirect

Journal of Luminescence

journal homepage: www.elsevier.com/locate/jlumin

Investigating the impact of gamma radiation on structural and optical properties of Eu^{3+} doped rare-earth hafnate pyrochlore nanocrystals

Victoria Trummel[a], Santosh K. Gupta[a,b], Madhab Pokhrel[a], Donald Wall[c], Yuanbing Mao[a,d,*]

[a] Department of Chemistry, University of Texas Rio Grande Valley, 1201 West University Drive, Edinburg, TX 78539, USA
[b] Radiochemistry Division, Bhabha Atomic Research Centre, Trombay, Mumbai 400085, India
[c] Nuclear Science Center, Washington State University, Pullman, WA 99164, USA
[d] School of Earth, Environmental, and Marine Sciences, University of Texas Rio Grande Valley, 1201 West University Drive, Edinburg, TX 78539, USA

ARTICLE INFO

Keywords:
Europium
Gamma
Phase transition
Pyrochlore
Luminescence

ABSTRACT

A proposed method for treating nuclear high level radioactive (NHLW) is to encapsulate it in a matrix made of complex oxide materials, such as pyrochlores with the general formula $A_2B_2O_7$. Rare-earth hafnate pyrochlores have the potential to advance the current methods of NHLW disposal due to their robust chemical stability in radioactive environments, their high thermal stability, and their natural structural compatibility with radionuclide species. In this study, $RE_2Hf_2O_7$:Eu^{3+} (RE = Y, La, Pr, Gd, Er, Lu) nanoparticles synthesized by a molten salt method were exposed to highly energetic gamma-ray irradiation. $La_2Hf_2O_7$:Eu^{3+} and $Lu_2Hf_2O_7$:Eu^{3+} underwent the order pyrochlore-disorder fluorite structural phase transition after exposure to gamma-ray irradiation. There was a change in the O-Eu charge transfer band (CTB) position as a function of gamma-ray dose. There was no change in the local symmetry of the Eu^{3+} dopant in $Y_2Hf_2O_7$, $Gd_2Hf_2O_7$ and $Lu_2Hf_2O_7$, but in $La_2Hf_2O_7$:Eu^{3+} gamma-ray dose reduced the symmetry around the Eu^{3+}. For $Y_2Hf_2O_7$:Eu^{3+} and $La_2Hf_2O_7$:Eu^{3+}, the lifetime and emission intensity were found to degrade possibly due to creation of gamma ray-induced defects which provides non-radiative pathways. Regarding $Gd_2Hf_2O_7$:Eu^{3+}, the concentration of oxygen vacancy defects predominated over other defects leading to enhanced emission and lifetime after gamma-ray irradiation. This study is of utmost importance for the design of a robust rare earth hafnate pyrochlore to be used as a nuclear waste host or gamma-ray based scintillator material.

1. Introduction

Investigating a material's properties by irradiating with ionizing radiation such as gamma rays and X-rays has been the focal point of many research activities recently, most notably in the area of photoluminescence, thermoluminescence, and scintillation, etc [1–4]. Most of the work in these areas is focused on irradiating the materials with gamma radiation, observing the changes in optical properties, and investigating radiation stability, etc. Intensive work has been performed to explore the photoluminescent properties of a variety of materials which have been exposed to γ-rays, such as bismuth/erbium co-doped silica fibers [5], graphene and CdTe/CdS colloidal quantum dots [6–8], ZnO and SnO_2 nanoparticles [9,10], gadolinium oxysulfide nanophosphors (Gd_2O_2S-nanoparticles) [11], porous silicon [12], $NdPO_4$ [13] and doped phosphor and glass materials [14–16]. There exists an interesting class of inorganic materials with the $A_2B_2O_7$ composition, which exists in two structural variations: the ordered pyrochlore (OP) with *Fd*-3*m* space group and the disordered fluorite (DF) having *Fm*-3*m* space group. The stability of the $A_2B_2O_7$ pyrochlore structure is dependent on the ionic radius ratio (r_A/r_B) of the A and B site ions. If $r_A/r_B > 1.76$, the OP is not favored, instead the monoclinic structure will form [13]. The DF is favorable if the ionic radius of B^{4+} and A^{3+} is similar ($r_A/r_B < 1.46$). This is due to the tendency of the A^{3+} and B^{4+} cations to swap positions in the lattice, consequently leading to antisite defects. The detailed structure of both phases was studied and detailed by Subramanian et al. [17] There has been a significant increase in the number of research of $A_2B_2O_7$ materials due to their excellent thermomechanical stability, good catalytic efficiency, high ionic conductivity, unique magnetic properties [18], high efficiency as luminescence hosts [19,20], along with a strong resistance to amorphization under irradiation due to their intrinsic ability to swap A and B sites forming antisite defects [21]. These unique and exceptional properties grant these $A_2B_2O_7$ materials viablity for numerous applications, such as electro- and photo-catalysts [22,23], magnetic materials [24],

* Corresponding author at: Department of Chemistry, University of Texas Rio Grande Valley, 1201 West University Drive, Edinburg, TX 78539, USA.
E-mail address: yuanbing.mao@utrgv.edu (Y. Mao).

https://doi.org/10.1016/j.jlumin.2018.10.069
Received 19 July 2018; Received in revised form 3 September 2018; Accepted 7 October 2018
Available online 24 October 2018

phosphors [19,20], defect-induced fluorescent materials [25], scintillators [26], and nuclear waste hosts [27], etc.

A good nuclear waste host demands various suitable properties, such as high thermal stability, high chemical stability, good radiation stability, resistance to radiation-induced amorphization, and negligible leaching, etc. Due to the nature of radioactive decay, these materials must withstand radiation damage effects of long-lived fission products and actinides for thousands of years. Within this context, there has been much work towards studying the effects of ionizing radiation on $A_2B_2O_7$ materials and then investigating their properties such as structural, nuclear, and radiation tolerance, etc. Many previously reported works have studied the effect of gamma irradiation on pyrochlores, such as $Er_2Ti_2O_7$ pyrochlore irradiated with 400 KeV Ne^{2+} ion [28,29], $RE_2Ti_2O_7$ (RE = Yb, Er, Y, Gd and Sm) irradiated with 2.2 GeV ^{197}Au [30], $Lu_2Ti_2O_7$ irradiated with various types of ionizing radiations such as Ne, Ar and Xe [31], $La_2Zr_2O_7$ irradiated with X-rays and protons [32], $Gd_2Sn_2O_7$ and $Gd_2Hf_2O_7$ irradiated with 1 MeV Kr^+ [33], $Gd_2Hf_2O_7$ and $Gd_2Ti_2O_7$ irradiated with 400 KeV Ne^+ [34], and tantalate pyrochlore irradiated with 1 MeV Kr^+ [35]. Currently, there are few studies outlining the relationship of irradiation and radiation induced amorphization of these $A_2B_2O_7$ materials. Sickafus and his team found that $Er_2Ti_2O_7$ is amorphized by irradiation with swift heavy ions (Xe) at a low ion dose, while $Er_2Zr_2O_7$ remained crystalline to the highest dose of Xe ion irradiation [36]. Cameron et al. studied the short-range order in the disordering of stannate pyrochlores by swift heavy ion irradiation and reported a loss of the initial pyrochlore structure due to electronic excitation-induced phase transformations [37]. Xia and colleagues synthesized $Lu_{2-x}Ce_xTi_2O_7$ (x = 0–0.7) and implanted it with 400 keV Ne^{3+} ions and revealed that the radiation tolerance decreased with increasing Ce content [38]. Souliè et al. found that when exposed to swift heavy on radiation and low mass ion irradiation, $Y_2Ti_2O_7$ pyrochlores with increasing displacements per cation (dpc) underwent the order to disorder phase transformation eventually evolving into an amorphous phase [39]. Nuclear high-level wastes (NHLW) contain most of the radioactivity generated during normal reactor operation. Because of the radioactive components present in the NHLW, the borosilicate glass or proposed $A_2B_2O_7$ type ceramic pyrochlore materials experience constant irradiation with α, β and γ radiation. Most reported literature is limited to ion beam irradiation as discussed above and none, to the best of our knowledge, have done systematic studies on the effect of different doses of gamma radiation on $A_2B_2O_7$ materials. Additionally, many previously reported studies are typically limited to titanates and zirconates with very few studies on Ne^+ and Kr^+ irradiated $Gd_2Hf_2O_7$ [33,34].

The $RE_2Hf_2O_7$ possess a unique set of properties that place them in high demand for use in innovative high-energy radiation detectors. Such properties include a high stopping power for X- and γ-rays with Z_{Hf} = 72 and a high density of 7.9 g/cm^3. They have also been investigated for use as a ceramic material for thermal barrier coatings [40], nuclear waste host [41–43] and as neutron absorbers in nuclear reactors [44]. Despite their countless exceptional properties, $RE_2Hf_2O_7$ hafnates have not gained as much recognition as titanates and zirconates. When exposed to gamma irradiation, $A_2B_2O_7$ materials can undergo disordering, phase transitions, defect formation, and amorphization, etc. When doped with RE^{3+} elements, such as Eu^{3+}, these rare-earth hafnates have a capacity to luminesce, creating the added potential for use in solid-state lighting, display devices, optical telecommunication components, active parts in lasers and bio-labels [45]. The doped europium ion was utilized as local structural probe to investigate the gamma radiation damage in these rare earth hafnates in more detail. Such changes can be easily discerned in the europium emission spectra. Not only is the photoluminescence spectra of europium well studied, it has several favorable features for interpretation of the local host environment, such as having a pure magnetic dipole transition ($^5D_0 \rightarrow {}^7F_1$) and a hypersensitive electric dipole $^5D_0 \rightarrow {}^7F_2$ transition. Due to the similar ionic radius and oxidation state, the trivalent RE ions could act as radioactive surrogates for the trivalent minor actinides such as Am, Cm, and Np because Eu^{3+} can mimic minor actinides, that is to say, Am and Cm. For the first time, a series of europium-doped rare-earth hafnates $RE_2Hf_2O_7$ (RE = Y, La, Pr, Gd, Er, and Lu) nanocrystals (NCs) have been systematically investigated before and after gamma-ray irradiation in this study. Phase pure rare-earth hafnate NCs were synthesized using a facile and low temperature combined coprecipitation and molten-salt synthesis (MSS) method. In MSS, the used molten salt plays an important role in determining the formation temperature and the reaction kinetics of products [46]. The use of molten salt brings down the formation temperature by increasing the contact area and transport kinetics between the reacting species compared with the traditional solid-state synthesis. Particle growth is normally governed by the Ostwald ripening mechanism, i.e. the particles which are too small or big than those with the critical value get dissolved in the used molten salt. The advantages of the MSS include low synthesis temperature, monodispersed nanoparticles, and particle size tunability by the coprecipitation pH, MSS duration and temperature [43,45–48]. The compositions tested in this study were yttrium, lanthanum, praseodymium, gadolinium, erbium and lutetium hafnates. The structural changes in $RE_2Hf_2O_7$:Eu^{3+} (RE = Y, La, Pr, Gd, Er, and Lu) unexposed and after exposure to different doses of gamma ray (800, 3200, and 12800 Gy) have been explored through X-ray diffraction and Raman spectroscopy. Other changes, such as defects, disorder, symmetry, and phase, etc., are explored using the europium luminescence through emission and lifetime spectroscopy. Such changes were further correlated with Judd-Ofelt analysis.

2. Experimental

The used starting materials include RE nitrate hexahydrate (RE $(NO_3)_3{\cdot}6H_2O$, analytical grade, 99.0%, RE = Y, La, Pr, Gd, Er, and Lu), hafnium dichloride oxide ($HfOCl_2{\cdot}xH_2O$, 99.9%), europium(III) nitrate hexahydrate ($Eu(NO_3)_3{\cdot}6H_2O$, 99.9%), potassium nitrate (KNO_3, 99.9%), sodium nitrate ($NaNO_3$, 98%) and ammonium hydroxide (NH_4OH, 28.0–30.0%). All materials were purchased from Sigma Aldrich and used without further purification.

These rare-earth hafnate NCs were synthesized following a previously reported method [19,20,27,49]. More specifically, the synthesis of $RE_2Hf_2O_7$:5%Eu^{3+} NCs (RE = Y, La, Pr, Gd, Er, and Lu) was accomplished by a two-step process. In the first step, a single-source complex precursor of $RE(OH)_3$0.5%$Eu(OH)_3{\cdot}HfO(OH)_2{\cdot}nH_2O$ was prepared via a co-precipitation route. In a typical synthesis process, 5(1-x) mmol RE hexahydrate, 5 mmol hafnium dichloride oxide hydrate, and 0.25 mmol europium (III) nitrate hexahydrate were dissolved in 200 mL of deionized water to form a clear solution. Then a 200 mL of dilute ammonia solution with a concentration of 10% was slowly dropped into the above metal nitrate solution under magnetically stirring. After agitation and aging for 3 h, the formed white precipitate was collected by centrifugation and washed with deionized water several times. Finally, the single-source complex precursor of 95%$RE(OH)_3$0.5%$Eu(OH)_3{\cdot}HfO(OH)_2{\cdot}nH_2O$ was dried at 110 °C overnight. In the second step, $RE_2Hf_2O_7$:5 mol%Eu^{3+} NPs were synthesized through a facile MSS process using the single-source complex precursors of $RE(OH)_3$0.5 mol %$Eu(OH)_3{\cdot}HfO(OH)_2{\cdot}nH_2O$ and nitrate mixture ($NaNO_3$:KNO_3 = 1:1, molar ratio) at 650 °C for 6 h.

X-ray diffraction (XRD) was utilized to check the crystallographic phase of these NCs. XRD patterns were collected using the Bruker D8 ADVANCE X-ray diffractometer with Cu $K\alpha_1$ radiation (λ = 0.15406 nm). The XRD patterns were collected utilizing a scanning mode of 2θ ranging from 10° to 90° with a scanning step size of 0.04° and a scanning rate of 0.1° min^{-1}. Raman spectroscopy was collected to differentiate the pyrochlore and fluorite crystal phases. Raman spectra were collected using the Bruker Senterra-system using a 785 nm helium-neon laser with a spatial resolution of 2 μm. Raman spectroscopy was collected within the range of 200–1000 cm^{-1}. To avoid

interference with the luminescence of Eu^{3+}, samples were excited at 785 nm. Photoluminescence spectra were collected to utilize the europium dopant as a spectroscopic probe of the local host environment into the $RE_2Hf_2O_7$:Eu^{3+} system. Luminescent emission spectra, excitation spectra, decay and quantum yield were collected using the Edinburgh Instruments FLS 980 spectrometer at room temperature. The entire system was controlled through the Edinburgh Instruments F980 data acquisition software. Excitation and emission spectra were corrected for the spectral sensitivity of the system and the detector as well as the intensity variation of the Xe light-source using a reference diode. All samples were excited at 254 nm using the Xenon Lamp source. In addition, the photoluminescence decay of the emission intensity as a function of time was measured utilizing a pulsed Xenon flash-lamp excitation source. The pulse width of the source was approximately 2 μs and the wavelength was controlled by the excitation monochromator. The collected decay curve was analyzed using Exponential Fit Analysis software provided by Edinburgh Instruments.

To investigate the effects of γ-ray radiation on crystal structure and luminescent properties of these $RE_2Hf_2O_7$:Eu^{3+} NCs, the as-prepared $RE_2Hf_2O_7$:5%Eu^{3+} NCs were exposed to 800, 3200, and 12800 Gy (Gy) of gamma-ray irradiation using 600 Ci (Co-60 source) gamma-irradiation facility at Nuclear Science Center of Washington State University (WSUNRC Co-60 Irradiation Facility). The doses were determined based on calibration using Fricke Dosimeter method [50]. Consequently, the dose values are not converted to doses in materials other than water. In practice, it is difficult to convert the Fricke results into doses to other materials, especially solids. Calibration of the Co-60 source was carried out by Fricke dosimetry [50]. After treated with specific doses of γ-ray radiation, these samples were further characterized with techniques described above.

3. Results and discussion

3.1. X-ray diffraction

XRD patterns (Fig. 1) from all unexposed $RE_2Hf_2O_7$:Eu^{3+} nanocrystalline samples displayed typical peaks associated with the fluorite structure (JCPDS No 17-0450) due to the insensitivity of XRD to the superlattice reflections of $A_2B_2O_7$ materials corresponding to their (111), (113) and (331) peaks. XRD data suggested that the $Y_2Hf_2O_7$:Eu^{3+}, $Pr_2Hf_2O_7$:Eu^{3+}, $Gd_2Hf_2O_7$:Eu^{3+} and $Er_2Hf_2O_7$:Eu^{3+} NCs maintained a stable crystal structure throughout the irradiation process even after the highest dose of 12,800 Gy, while the $La_2Hf_2O_7$:Eu^{3+} and $Lu_2Hf_2O_7$:Eu^{3+} NCs displayed the most severe structural changes after γ-ray exposure. No evidence of amorphization could be seen in any of the samples even after 12,800 Gy. When comparing these rare-earth hafnates to prevalent competing compositions such as titanates, which undergo radiation-induced amorphization even at very low fluences [34] due to the significant disparity in the ionic radii of the RE^{3+} and Ti^{4+} ions, hafnates can withstand amorphization at much higher fluences due to the proximity in the ionic radii of the RE^{3+} and Hf^{4+} ions. As a result, rare-earth hafnates could form antisite defects by swapping A and B sites giving hafnates $RE_2Hf_2O_7$ the ability to dissipate excess radiation energy by forming these antisite defects.

The lattice parameters of the $La_2Hf_2O_7$:Eu^{3+} and $Lu_2Hf_2O_7$:Eu^{3+} NCs increased with increasing γ-ray irradiation. Such changes can be attributed to structural reorganization of the nanoparticles which in turn leads to a change in lattice parameters and unit cell volume due to crystal minimization on impact with high energy γ-ray radiation [9]. Additionally, lanthanum and lutetium hafnates experienced a shift of the most intense peak (2θ = 30°) to low angle after exposure of 800 and 3200 Gy, and then back to the initial structure after exposure to 12,800 Gy. There may have been a γ-ray radiation-induced unit cell expansion-contraction phenomenon taking place wherein the lattice cell expands at a low dose and then again contracts at a higher dose. Expansion or compression of crystal lattice under gamma irradiation has already been noticed in different nanostructures [51,52].

The average particle size was calculated using Scherer's equation and is shown in Table 1. There was very little change in the crystallite size caused by the γ-ray irradiation for the $Y_2Hf_2O_7$:Eu^{3+}, $Pr_2Hf_2O_7$:Eu^{3+}, $Gd_2Hf_2O_7$:Eu^{3+} and $Er_2Hf_2O_7$:Eu^{3+} NCs. Interestingly, the crystallite size of the $La_2Hf_2O_7$:Eu^{3+} and $Lu_2Hf_2O_7$:Eu^{3+} NCs increased after 800 and 3200 Gy then recrystallized back to a comparable size as unexposed under irradiation with highest dose of 12.8 kGy. The $Lu_2Hf_2O_7$:Eu^{3+} NCs also exhibited a very distinct characteristic from other rare-earth hafnates. The peak corresponding to 2θ = 30°, 34°, 50° and 58° underwent splitting into two sub-peaks after exposure to a low dose of 800 Gy. The changes depicted in $Lu_2Hf_2O_7$ after exposure to 800 and 3200 Gy were much more severe than those seen in $La_2Hf_2O_7$:Eu^{3+}. Peak splitting can be seen that may be potentially depicting the order-disordered transition or stabilization of the low symmetry phase. Peaks were analyzed using the JCPDS database, and no exact matches were found. It can be inferred that this sample is potentially composed of a mixture of the two phases or an intermediate phase undergoing the order-disorder phase transformation, sometimes referred as the defect pyrochlore phase [53]. After exposure to 3200 Gy, $Lu_2Hf_2O_7$:Eu^{3+} completely transitioned into the pyrochlore phase. After exposure to 12,800 Gy, $Lu_2Hf_2O_7$:Eu^{3+} transitioned back into the original fluorite phase indicating that this sample was not stable under all doses of γ-ray irradiation. This ordered to disordered phase transformation of $La_2Hf_2O_7$:Eu^{3+} and $Lu_2Hf_2O_7$:Eu^{3+} after exposure to γ-ray radiation is of interest for further studying the effects of radiation on this transformation process in future works.

3.2. Raman spectra

Raman spectroscopy is frequently utilized to distinguish between the fluorite and pyrochlore crystalline phases of $A_2B_2O_7$ type compositions. According to group theory, the ordered pyrochlore phase possesses a total of six Raman active vibrational modes existing in the range of 200–1000 cm^{-1} which are $\Gamma = A_{1g} + E_g + 4\ F_{2g}$ while the defect fluorite structure has only one active mode that is $\Gamma = F_{2g}$ [54,55]. In the ordered $A_2B_2O_7$ pyrochlore structure, the six Raman peaks are exclusively associated with the two different spatially localized oxygen ions O(48f) and O(8b). The metal-oxygen (at the 48f position) bonds are related to the A_{1g}, E_g and 3 F_{2g} vibrational modes whereas the metal-oxygen (at the 8b position) bonds are related to the F_{2g} vibrational modes [56]. And its RE^{3+} and Hf^{4+} ions are localized at 16*d* and 16*c* sites, respectively, and are Raman inactive since they are situated at centrally symmetric positions. In the disordered $A_2B_2O_7$ fluorite structure, the seven O^{2-} ions are randomly distributed over the 8 anionic sites in this structure, giving rise to significant disordering and thus typically giving a single broad Raman peak. The ionic radius ratio (r_A/r_B) is a critical factor in determining the type of crystal structure that an $A_2B_2O_7$ lattice will preferably adopt [17]. Usually the DF to OP transformation takes place when $r_A/r_B \sim 1.46$. Based on recent studies, it was predicted that r_A/r_B for the different $RE_2B_2O_7$ compositions followed this pattern: DF $r_A/r_B < 1.21 < \delta$-phase $r_A/r_B < 1.42 - 1.44 <$ OP $r_A/r_B < 1.78 - 1.83 <$ monoclinic pyrochlore $r_A/r_B < 1.92$ [57]. Based on the aforementioned pattern of the r_A/r_B, $Y_2Hf_2O_7$:Eu^{3+}, $Er_2Hf_2O_7$:Eu^{3+}, and $Lu_2Hf_2O_7$:Eu^{3+} are expected to form the defect-fluorite structures, and $La_2Hf_2O_7$:Eu^{3+}, $Pr_2Hf_2O_7$:Eu^{3+}, $Gd_2Hf_2O_7$:Eu^{3+} are expected to stabilize in ordered pyrochlore phase. Table 2 depicts the radius ratio for 8-coordinated A and 6-coordinated B site for various rare earth hafnate compositions and the expected structures.

From the Raman spectra (Fig. 2) taken from these $RE_2Hf_2O_7$:Eu^{3+} (RE = Y, La, Pr, Gd, Er and Lu) samples, unexposed $Y_2Hf_2O_7$:Eu^{3+}, $Gd_2Hf_2O_7$:Eu^{3+} and $Lu_2Hf_2O_7$:Eu^{3+} NCs (Fig. 2a, d, and f) displayed a single broad band typical of the DF structure due to the random distribution of the seven oxygen ions at the eight anionic sites. Although $Gd_2Hf_2O_7$:Eu^{3+} was expected to stabilize in ordered pyrochlore phase,

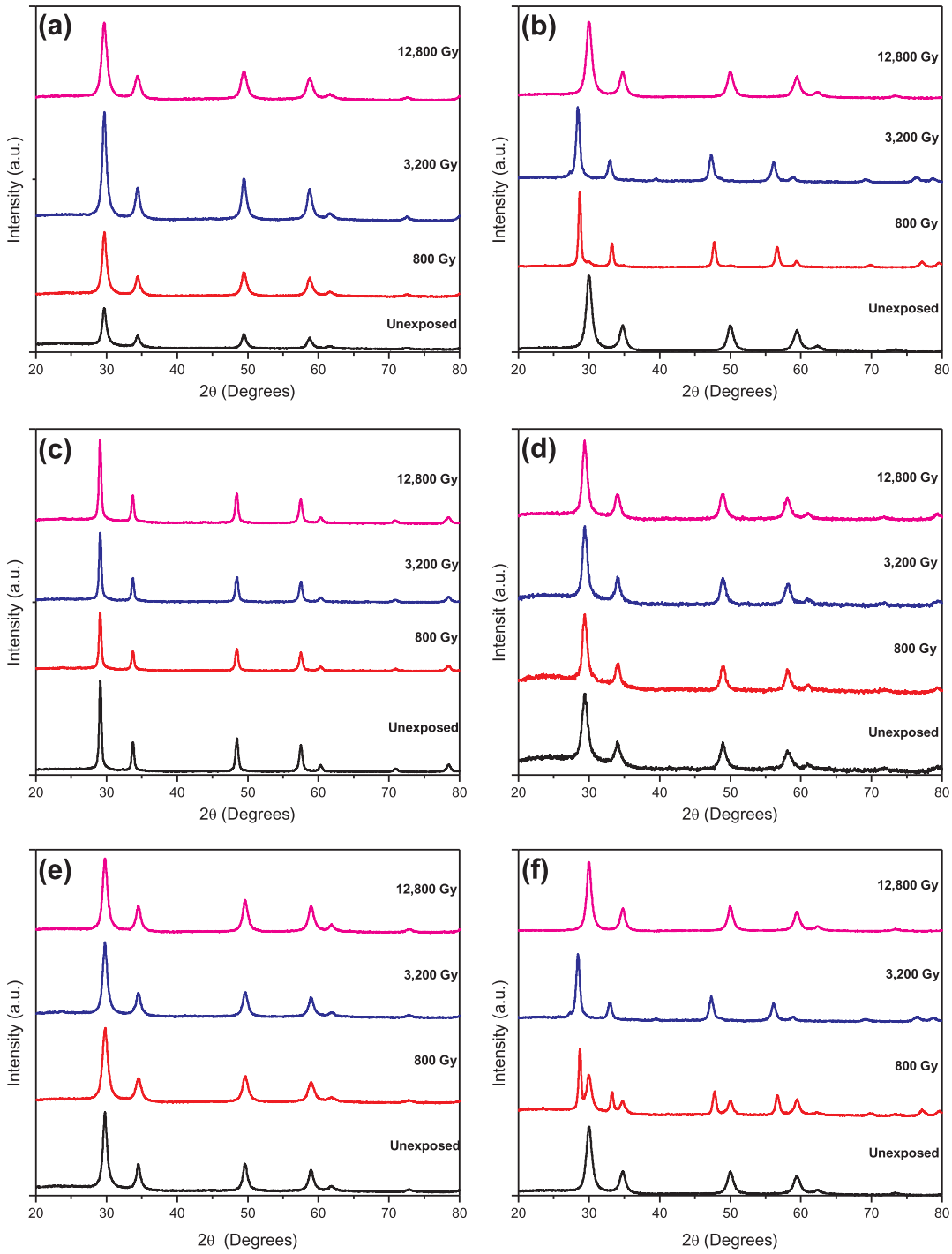

Fig. 1. XRD patterns of the 5.0 mol% Eu^{3+} doped: (a) $Y_2Hf_2O_7$, (b) $La_2Hf_2O_7$, (c) $Pr_2Hf_2O_7$, (d) $Gd_2Hf_2O_7$, (e) $Er_2Hf_2O_7$, and (f) $Lu_2Hf_2O_7$ NCs before and after γ-ray irradiation with doses of 800, 3200 and 12,800 Gy (Gy).

Table 1
Calculated particle size of the $RE_2Hf_2O_7$:5 mol%Eu^{3+} NCs before and after γ-ray irradiation using Scherer's equation based on XRD data shown in Fig. 1.

γ-ray dose (Gy)	Calculated particle size (nm) of the $RE_2Hf_2O_7$:5 mol%Eu^{3+} NCs					
	RE = Y	RE = La	RE = Pr	RE = Gd	RE = Er	RE = Lu
0	12.63	9.24	22.87	8.45	12.62	9.36
800	12.16	20.24	22.35	10.74	9.69	23.93
3200	12.82	14.59	22.01	10.69	12.04	13.93
12,800	9.61	9.46	21.77	10.61	10.90	10.09

Table 2
Ionic radius ratio for 8-coordinated A and 6-coordinated B site for various $A_2B_2O_7$ composition and the expected structure.

Rare earth hafnate	r_A/r_B	Expected phase based on radius ration
$Y_2Hf_2O_7$:Eu^{3+}	1.26	Defect Fluorite
$La_2Hf_2O_7$:Eu^{3+}	1.45	Ordered Pyrochlore
$Pr_2Hf_2O_7$:Eu^{3+}	1.39	Ordered Pyrochlore
$Gd_2Hf_2O_7$:Eu^{3+}	1.32	Ordered Pyrochlore
$Er_2Hf_2O_7$:Eu^{3+}	1.25	Defect Fluorite
$Lu_2Hf_2O_7$:Eu^{3+}	1.21	Defect Fluorite

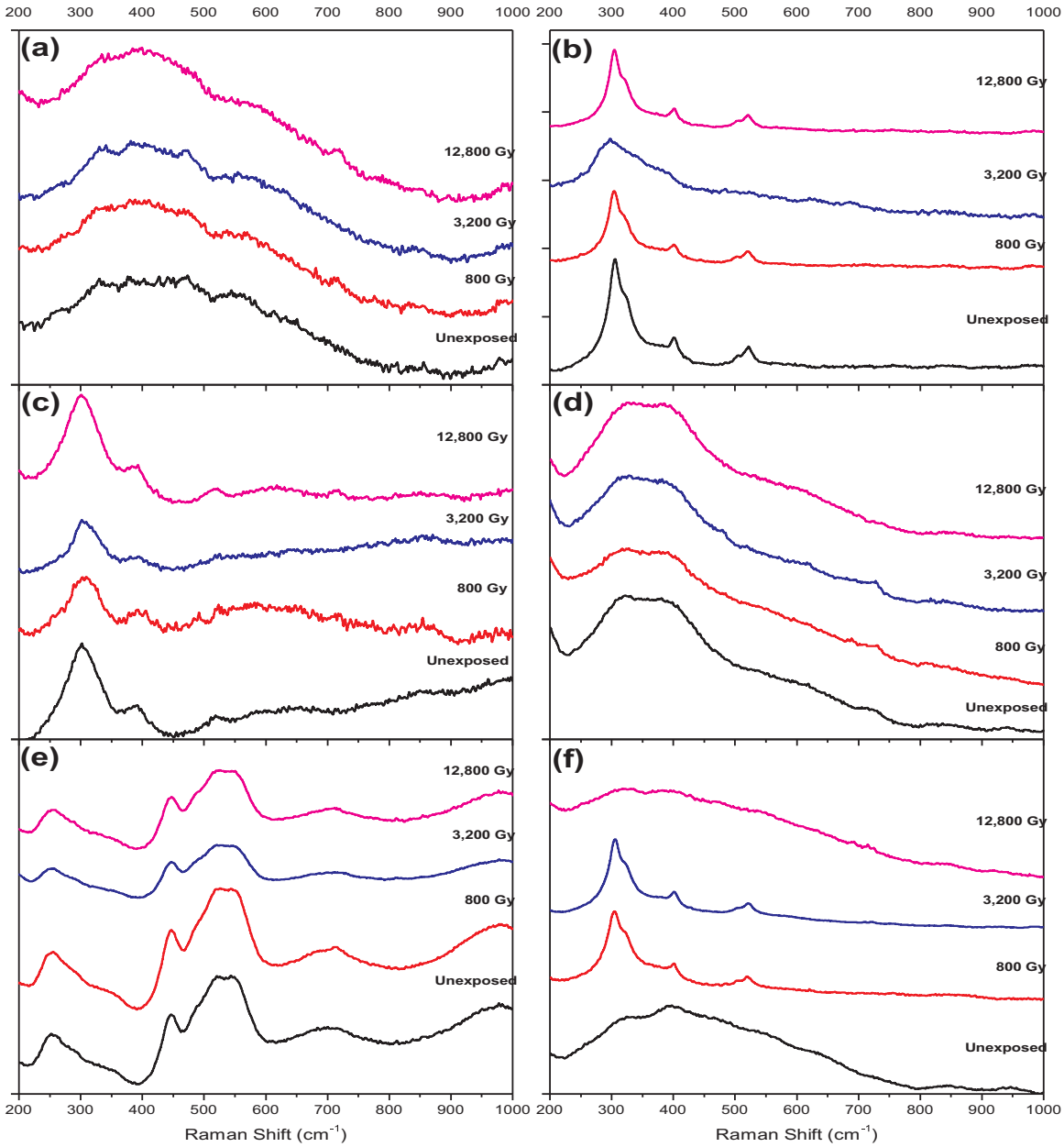

Fig. 2. Raman spectra of the 5.0 mol% Eu^{3+} doped (a) $Y_2Hf_2O_7$, (b) $La_2Hf_2O_7$, (c) $Pr_2Hf_2O_7$, (d) $Gd_2Hf_2O_7$, (e) $Er_2Hf_2O_7$, and (f) $Lu_2Hf_2O_7$ NCs before and after γ-ray irradiation with doses of 800, 3200 and 12,800 Gy (Gy).

six well-resolved Raman modes were not observed for this composition. On the other hand, the unexposed $La_2Hf_2O_7$:Eu^{3+} NCs displayed (Fig. 2b) six well-resolved pyrochlore vibrational modes of E_g (322 cm^{-1}), A_{1g} (503 cm^{-1}) and 4 F_{2g} (305 cm^{-1} as the main peak, 401, 521 and 750 cm^{-1} as a very weak peak) in the Raman spectrum. This is consistent with its ionic radius ratio (r_{La}/r_{Hf}). The Raman spectrum of the unexposed $Pr_2Hf_2O_7$:Eu^{3+} (Fig. 2c) displayed features wherein four F_{2g} modes (300, 389, 519 and 750 cm^{-1}) were well resolved and distinct, but the E_g and A_{1g} modes overlaped with the first and third F_{2g} modes, respectively. The Raman peaks of the $Pr_2Hf_2O_7$:Eu^{3+} sample shifted and broadened significantly compared to those of the $La_2Hf_2O_7$:Eu^{3+} sample. This may be attributed to the increased atomic number and decreased ionic radius ratio which lead to additional disordering in the pyrochlore anionic sublattice [56]. For the $Er_2Hf_2O_7$ sample, its Raman spectrum contained peaks (Fig. 2e) positioned at 250, 344, 445, 519, 546, 682 and 970 cm^{-1}. It is difficult to distinguish whether it has the fluorite or pyrochlore structure. When comparing it with the Raman spectra of $La_2H_f2O_7$:Eu^{3+} (with pyrochlore structure) (Fig. 2b), these peaks of the $Er_2Hf_2O_7$:Eu^{3+} sample could be attributed to the Raman vibrational modes to E_g (at 344 cm^{-1}) whereas F_{2g} (445 and 519 cm^{-1}) although the peaks are highly shifted and broadened compared to those of the $La_2Hf_2O_7$:Eu^{3+} sample. This may be due to increased disorder induced by the higher atomic number of the erbium ion. The extra Raman peaks at 250 and 970 cm^{-1} could be attributed to distortion in HfO_6 (breathing mode). The broad Raman band at 546 cm^{-1} can be attributed to the A_{1g}/F_{2g}. On the other hand, highly broad Raman peaks at 672 cm^{-1} were attributed to the rare earth ion coordinated to 7 oxygen ions as observed in the disordered fluorite phase [58]. It has been reported that in a completely disordered defect-fluorite phase, individual Raman modes would be indistinguishable. All the spectra for the $Er_2Hf_2O_7$:Eu^{3+} NCs with all gamma doses (Fig. 2e) indicate some initial pyrochlore-type short-range ordering of cations and oxygen vacancies with features that are more likely to justify the disorder fluorite crystal structure of the

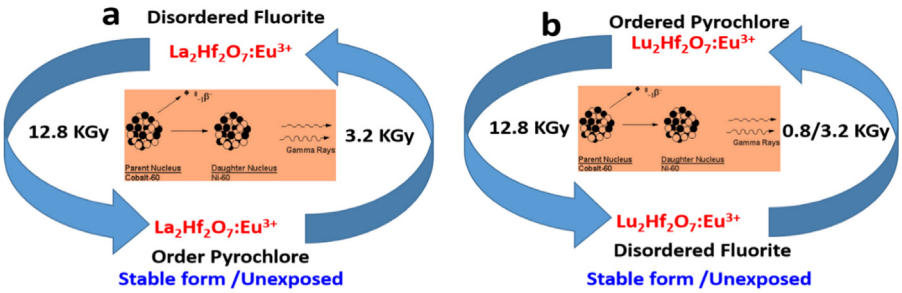

Fig. 3. Schematics depicting the effect of γ-ray irradiation on the crystallographic structure of the $La_2Hf_2O_7$:5 mol%Eu^{3+} and $Lu_2Hf_2O_7$:5 mol%Eu^{3+} NCs.

$Er_2Hf_2O_7$:Eu^{3+} NCs [54,58,59].

As far as the effect of γ-ray radiation is concerned, the structural features of the $Y_2Hf_2O_7$:Eu^{3+}, $Pr_2Hf_2O_7$:Eu^{3+}, $Gd_2Hf_2O_7$:Eu^{3+}, and $Er_2Hf_2O_7$:Eu^{3+} NCs remained intact, even after being irradiated with 12,800 Gy. However, similarly to what was observed in the XRD data in terms of change in lattice parameter and crystallite size, the $La_2Hf_2O_7$:Eu^{3+} and $Lu_2Hf_2O_7$:Eu^{3+} samples displayed structural changes after exposure to γ-ray irradiation. Specifically, based on the Raman spectra from the $La_2Hf_2O_7$:Eu^{3+} sample (Fig. 2b), no changes could be seen after 800 Gy irradiation, but there may be a structural phase transition from ordered pyrochlore to disordered fluorite after 3200 Gy irradiation. At even higher γ-ray doses, e.g. 12,800 Gy, a structural reorganization to order pyrochlore structure took place. For the $Lu_2Hf_2O_7$:Eu^{3+} sample, which originally stabilized at disordered fluorite structure due to $r_A/r_B = 1.21$, this sample transformed into the ordered pyrochlore structure after exposure to 800 Gy and 3200 Gy of γ-ray radiation then reoriented back to the fluorite phase after 12,800 Gy irradiation. Fig. 3 schematically depicts how their structure changed after γ-ray irradiation. This fascinating behavior is only displayed by lanthanum (f^0) hafnate and lutetium (f^{14}) hafnate – two extreme compositions which have the maximum and minimum ionic radius ratio r_{RE}/r_{Hf} of the samples in this study. In pyrochlores, structural changes are known to takes place under high pressure, high temperature, and under ion irradiation [54]. Most studies of radiation induced structural changes in pyrochlores dealt with alpha radiation only [60,61]. Lang et al. have observed radiation (mostly alpha) induced amorphization in titanate pyrochlores, whereas the zirconate pyrochlore did not amorphize, but rather it underwent a phase transition to the defect-fluorite structure. Under ion beam irradiation, defects like cation antisite and anion Frenkel pair defects are formed in $A_2B_2O_7$ pyrochlores [61]. The accumulation of these defects drives the pyrochlore-to-fluorite and crystalline to-amorphous structural transformations.

3.3. Photoluminescence spectra

Among all the lanthanide (Ln^{3+}) ions, the Eu^{3+} ion is considered to be one of the most extensively used spectroscopic probes due to its non-degenerate emissive ($^5D_0$) and the ground state $^7F_0$. The $^5D_0 \rightarrow {}^7F_2$ transition of Eu^{3+} is an electric-dipole (ED) one, which is hypersensitive to the local site symmetry, whereas the $^5D_0 \rightarrow {}^7F_1$ transition is a magnetic-dipole (MD) one, which is insensitive to the local site symmetry. The symmetry around a lanthanide ion can thus be deduced from the shape of the emission spectrum of the Eu^{3+} ion. The sharp-line spectra of the Eu^{3+} ion and non-degenerate $^5D_0$ emissive state, wherein the spectrum displays unique electric and magnetic dipole moment due to $^5D_0 \rightarrow {}^7F_2$ and $^5D_0 \rightarrow {}^7F_1$ respectively, can give detailed information about the surroundings of the Eu^{3+} ion in the host lattice [62]. In fact, spectral splitting in its $^5D_0 \rightarrow {}^7F_0$ transition, which is magnetically as well electrically forbidden, gives information about the number of metal ion sites [63]. Extensive work has been done in previous studies on europium doped $A_2B_2O_7$ materials in several compositions such as $Gd_2Zr_2O_7$, $Nd_2Zr_2O_7$, $RE_2Hf_2O_7$ and deciphered information such as the local structure (A or/and B site), and point group symmetry, etc [19,49,63–65].

In this study, excitation, emission, and decay of photoluminescence (Figs. 4, 5 and 7, respectively) were measured for these Eu^{3+} doped hafnates $RE_2Hf_2O_7$:Eu NCs (i) to investigate their optical property changes after exposure to γ-ray radiation at various doses and (ii) to compare how their luminescent properties changed depending on various $RE_2Hf_2O_7$ hosts with RE = Y, La, Gd and Lu. The $Y_2Hf_2O_7$:Eu^{3+}, $La_2Hf_2O_7$:Eu^{3+}, $Gd_2Hf_2O_7$:Eu^{3+}, and $Lu_2Hf_2O_7$:Eu^{3+} samples showed typical emission and excitation curves associated with the presence of Eu^{3+} within the crystal lattice. On the contrary, the $Pr_2Hf_2O_7$:Eu^{3+} and $Er_2Hf_2O_7$:Eu^{3+} NCs did not show spectral characteristics within this range. This could potentially be due to the absence of energy transfer from the host to the europium ion caused by a mismatch in energy levels of these hosts with the europium ion. However, energy transfer from host to dopant ions is not the sole reason for observing Eu^{3+} luminescence. Phonon energy and the value and position of band gap of the host also play important roles. Even after the excitation of the Eu^{3+} f-f band (395 nm), no characteristic emission of Eu^{3+} was observed from the $Pr_2Hf_2O_7$:Eu^{3+} and $Er_2Hf_2O_7$:Eu^{3+} NCs even though our EDX analysis confirmed its presence. In general, to observe Eu^{3+} luminescence, the Eu 4f states must fit in the bandgap of the host compound. However, when either Eu^{3+} 4f ground states overlap with the valence band or Eu 4f excited states overlap with the conduction bands of hosts, Eu^{3+} will not show luminescence even if adequate doping has been achieved. The valence band of these $A_2Hf_2O_7$ hosts is composed of O (2p) and the conduction band is mixed from Hf (5d) and Er (5d) or Pr (5d) states. There are only a few literature reports available comparing the bandgaps of these $A_2Hf_2O_7$ hosts. For example, Zu et al. compared the bandgaps of $Er_2Hf_2O_7$ (2.946 eV) and $La_2Hf_2O_7$ (5.6 eV) [66]. The small bandgap of $Er_2Hf_2O_7$ could enable Eu 4 f excited states lying above its conduction band, which prevents the luminescence from Eu^{3+} doped in the $Er_2Hf_2O_7$ host. However, there is no reported data regarding this phenomenon for $Pr_2Hf_2O_7$, so additional experiments are necessary to confirm this proposed explanation in the future.

Fig. 4 shows the excitation spectra of $RE_2Hf_2O_7$:Eu^{3+} NCs (RE = Y, La, Gd, and Lu) under the emission wavelength of 612 nm corresponding to the $^5D_0 \rightarrow {}^7F_2$ transition of the Eu^{3+} ion. The excitation spectra for all the samples displayed a broad charge transfer band (CTB) in the range of 230–300 nm with a peak around 254 nm followed by a number of sharp peaks corresponding to of the f-f transition of Eu^{3+} ions. The broad CTB is assigned to the combined effect of various electronic transitions, i.e. $O_{2p} \rightarrow Eu_{4f}$, $O_{2p} \rightarrow Hf_{3d}$, and $Eu_{4f} \rightarrow Hf_{3d}$ charge transfer transitions with the predominant transition being the $O_{2p} \rightarrow Eu_{4f}$. The relatively sharp peaks from 350 to 500 are attributed to intra f-f transitions of the Eu^{3+} ion, specifically, 362 nm of $^7F_0 \rightarrow {}^5D_4$, 383 nm of $^7F_0 \rightarrow {}^5G_{2-4}$, 393 nm of $^7F_0 \rightarrow {}^5L_6$, 413 nm of $^7F_0 \rightarrow {}^5D_3$, and 465 nm of $^7F_0 \rightarrow {}^5D_2$. The near UV band at 393 nm and blue band at 465 nm are relatively more intense than other f-f bands. This suggests that these $RE_2Hf_2O_7$:Eu^{3+} (RE = Y, La, Gd, and Lu) phosphors can be effectively pumped by NUV light or blue LEDs.

The CTB of the $Y_2Hf_2O_7$:Eu^{3+} NCs (Fig. 4a) shifted from 249.4 nm to 251.2 nm after γ-ray exposure to 800 and 3200 Gy, then further red-

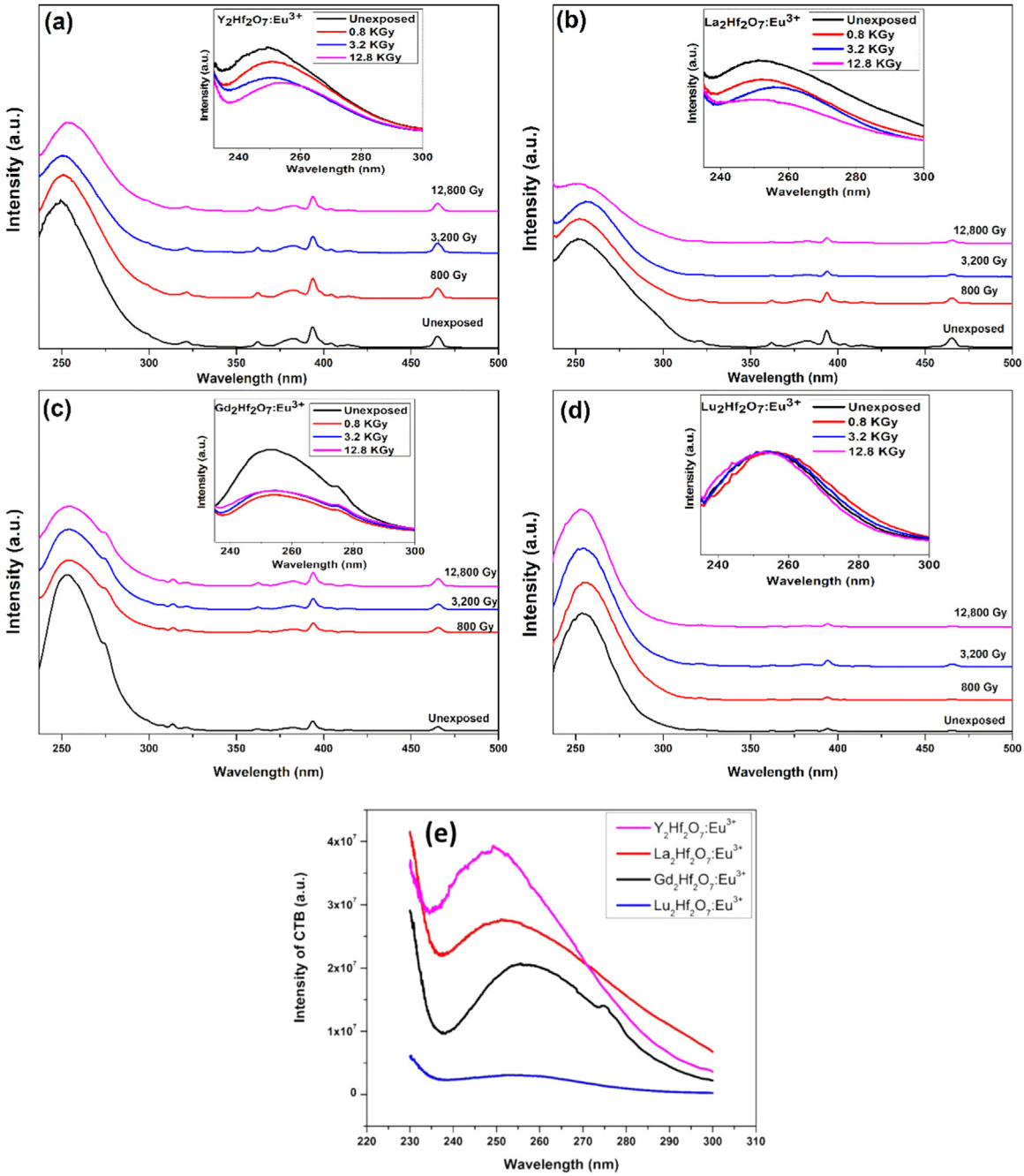

Fig. 4. Excitation spectra (λ_{em} = 612 nm) of the 5.0 mol% Eu^{3+} doped (a) $Y_2Hf_2O_7$, (b) $La_2Hf_2O_7$, (c) $Gd_2Hf_2O_7$, and (d) $Lu_2Hf_2O_7$ NCs before and after γ-ray irradiation with doses of 800, 3200 and 12,800 Gy. The average CTB was determined to be ~ 254 nm. Inset of all figures shows the magnified CTB region from 220 to 300 nm. (e) Position of CTB for the unexposed $RE_2Hf_2O_7$:5%Eu^{3+} NPs.

shifted to 253.3 nm after γ-ray exposure to 12800 Gy. This may be due to the γ-ray irradiation of this defect fluorite sample causing the creation of electron-hole pair and metastable defects (e.g. cation vacancies, oxygen vacancies, and interstitials, etc.). Moreover, because γ-rays are highly penetrating, their effect occurs throughout irradiated samples. As previously discussed, the CTB of the trivalent europium ions arises due to electronic transition from the O^{2-} to the Eu^{3+} ion. Metastable defects created by γ-ray irradiation facilitate such electronic transitions more efficiently by providing an intermediate level. Therefore, γ-ray irradiation of the Eu^{3+} ion will cause a stronger tendency to pull the electron from the O^{2-} ion leading to an increase of the covalency of the metal-oxygen (Eu–O). Hence, lower energy will be required for transferring the electron from the O^{2-} ion to the Eu^{3+} ion. As a result of all these phenomena, the charge transfer energy is reduced and a red-shift was observed.

The CTB of the $La_2Hf_2O_7$:Eu^{3+} NCs (Fig. 4b) did not exhibit any change after the γ-ray exposure to 800 Gy, but red-shifted from 251.1 nm to 255.5 nm after the γ-ray exposure to 3200 Gy, and then returned to the same peak position after the γ-ray exposure to 12,800 Gy. This phenomenon may be attributed to structural changes of the ordered pyrochlore transitioning to defect fluorite after the γ-ray exposure to 3200 Gy, as observed by the XRD and Raman studies (Figs. 1 and 2). Oxygen to europium charge transfer (O_{2p}→Eu_{4f}) requires less energy in the disordered fluorite $La_2Hf_2O_7$ compared to the ordered pyrochlore. This is mostly attributed to two factors: (a) larger unit cell and (b) high close packing fraction of ideal pyrochlore lattice

compared to disordered fluorite [17]. Therefore, there is a lower charge transfer energy for O_{2p}→Eu_{4f} transition depicted as redshifting in disordered fluorite after the γ-ray exposure to 3200 Gy. The occurence reverses after exposure to 12,800 Gy due to the crystallographic transition back to the ordered pyrochlore.

The CTB of the $Gd_2Hf_2O_7$:Eu^{3+} NCs (Fig. 4c) blue-shifted slightly from 257.4 nm to 256.9 nm after the γ-ray exposure to 800 Gy, then red-shifted to 258.3 after the γ-ray exposure to 3200 Gy, and then blue-shifted slightly to 258.1 nm after exposure to 12,800 Gy. As such, there is not much change in the structure of $Gd_2Hf_2O_7$:Eu^{3+} NCs as a function of gamma dose that can be seen from the Raman spectra (Fig. 2d). So these changes in the position of CTB can be attributed to formation of metastable defects (oxygen vacancies) due to gamma-ray irradiation. At the lowest and highest dose, the position of metastable defects in the host bandgap is not favorable for electronic transition whereas at intermediate dose it favors such transition.

The CTB of the $Lu_2Hf_2O_7$:Eu^{3+} NCs (Fig. 4d) initially red-shifted from 253.3 nm to 254.3 nm after exposure to 800 and 3200 Gy, and then blue-shifted back to 253.4 nm after exposure to 12,800 Gy. As previously mentioned, after the γ-ray exposure to 800 and 3200 Gy, the disorder fluorite $Lu_2Hf_2O_7$:Eu^{3+} NCs transitioned into the ordered pyrochlore phase (undergoing the disorder-order transition), and then reverted back to the disordered fluorite phase after exposure to 12,800 Gy. Such structural transitions are responsible for the CTB shifting of the $Lu_2Hf_2O_7$:Eu^{3+} NCs, similarly to what was observed for the $La_2Hf_2O_7$:Eu^{3+} sample (Fig. 4b). Another interesting phenomenon was the change in the position of CTB (unexposed) between different hosts. The CTB of unexposed sample is shown in Fig. 4e.

Specifically, the CTB peak changes from 249.4 nm of $Y_2Hf_2O_7$:Eu^{3+}, 251.1 nm of $La_2Hf_2O_7$:Eu^{3+}, 260.5 nm of $Gd_2Hf_2O_7$:Eu^{3+}, and finally to 253.4 nm of $Lu_2Hf_2O_7$:Eu^{3+}. Blasse suggested that the electrostatic potential at the O^{2-} ion is the one which decides the energy of the CTB [67], whereas Hoefdraad suggested that the energy of the CTB in some of the phosphors may be described based on Jorgensen's concept of optical electronegativity χ [68]. Based on expression formulated by Jorgensen [69], one can also predict the charge transfer energy using the equation:

$$E^{CT} = 3.72\,(\chi_X - \chi_M)\ \text{eV} \quad (1)$$

where χ_X is the optical electronegativity of the anion x (oxygen in this case) from where the electron is transferred, and χ_M is the optical electronegativity of the metal M (europium in this case) where the electron is being transferred. Here in this case differences arise possibly due to the difference in electronegativity of oxygen ion attached to different metal ions of Y^{3+}, La^{3+}, Gd^{3+}, and Lu^{3+}.

Fig. 5 shows the emission spectra of the $RE_2Hf_2O_7$:5%Eu^{3+} (RE = Y, La, Gd, and Lu) NCs excited at 254 nm. All the spectra displayed typical patterns characteristic of Eu^{3+} ions with peaks at 578, 591, 618, 653 and 709 nm due to the $^5D_0$→$^7F_0$, $^5D_0$→$^7F_1$ (magnetic dipole transition, MDT), $^5D_0$→$^7F_2$ (electric dipole transition, EDT), $^5D_0$→$^7F_3$ and the $^5D_0$→$^7F_4$, respectively. The intensity of the $^5D_0$→$^7F_1$ MDT is largely independent of the environment of the Eu^{3+} ion and often considered constant. The $^5D_0$→$^7F_2$ EDT is known as the "hypersensitive transition" because its intensity is largely influenced by the local symmetry of the Eu^{3+} ion and the nature of the ligands. The ratio of EDT/MDT known as asymmetry ratio can allude information about the local symmetry around the Eu^{3+} ion. The appearance of luminescent transitions of $^5D_0$→$^7F_0$ and $^5D_0$→$^7F_3$ has neither been explained by the magnetic dipole mechanism or Judd–Ofelt theory. In fact, their intensities are very weak and their presence in the emission spectra (Fig. 5a-d)

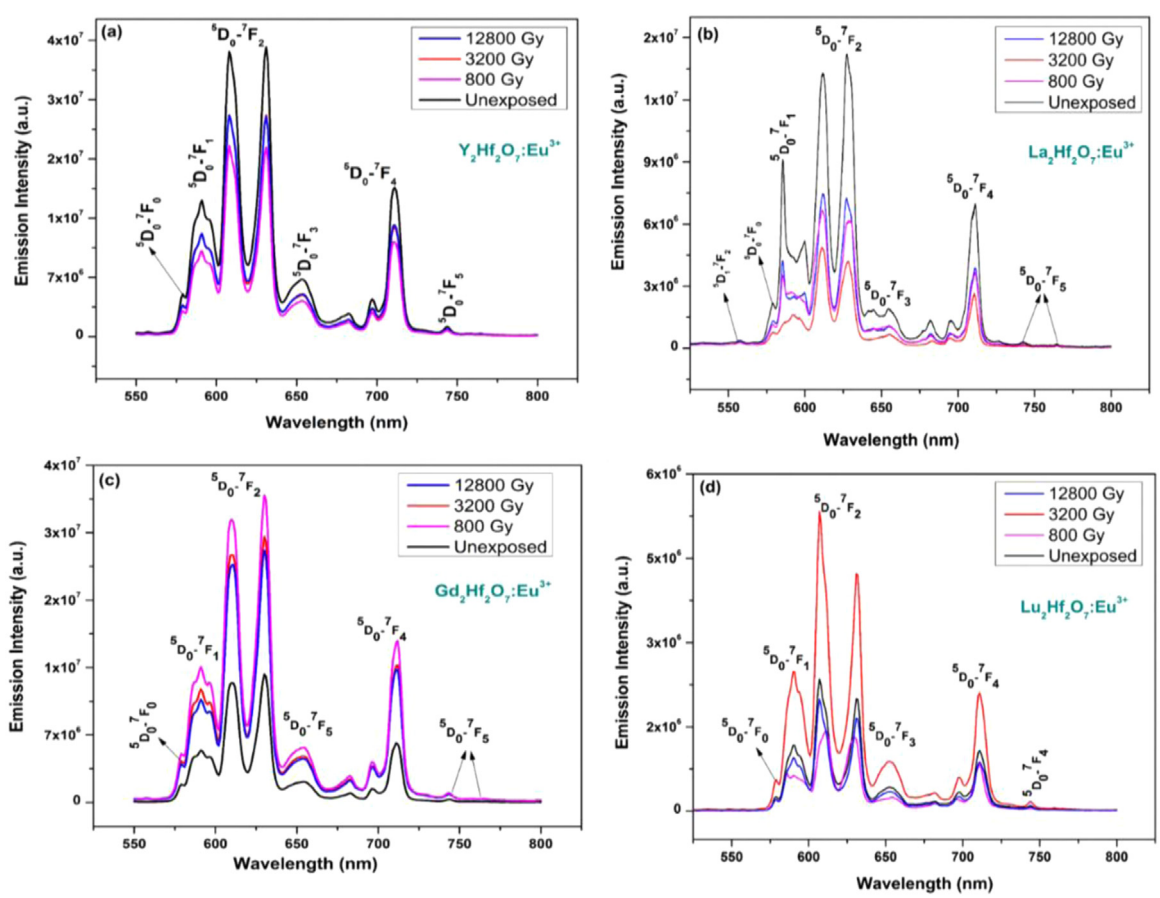

Fig. 5. Emission spectra of the 5 mol% Eu^{3+} doped (a) $Y_2Hf_2O_7$, (b) $La_2Hf_2O_7$, (c) $Gd_2Hf_2O_7$, and (d) $Lu_2Hf_2O_7$ NCs before and after γ-ray irradiation with doses of 800, 3200 and 12,800 Gy.

Table 3
Stark splitting components of each transition in the $RE_2Hf_2O_7:Eu^{3+}$ (RE = Y, La, Gd, and Lu) NCs.

	$^5D_0 \rightarrow {}^7F_0$	$^5D_0 \rightarrow {}^7F_1$	$^5D_0 \rightarrow {}^7F_2$	$^5D_0 \rightarrow {}^7F_3$	$^5D_0 \rightarrow {}^7F_4$	Point group symmetry
$Y_2Hf_2O_7:Eu^{3+}$						
Unexposed	1	3	2	2	4	C_{4v}
800 Gy	1	3	2	2	4	C_{4v}
3200 Gy	1	3	2	2	4	C_{4v}
12,800 Gy	1	3	2	2	4	C_{4v}
$La_2Hf_2O_7:Eu^{3+}$						
Unexposed	1	2	3	3	5	C_{3v}
800 Gy	1	3	3	1	4	C_{6v}
3200 Gy	1	3	3	1	3	C_6
12,800 Gy	1	3	3	2	5	C_6
$Gd_2Hf_2O_7:Eu^{3+}$						
Unexposed	1	3	2	2	3	C_6
800 Gy	1	3	2	2	3	C_6
3200 Gy	1	3	2	2	3	C_6
12,800 Gy	1	3	2	2	3	C_6
$Lu_2Hf_2O_7:Eu^{3+}$						
Unexposed	1	3	3	1	3	C_6
800 Gy	1	2	3	1	3	C_6
3200 Gy	1	3	3	1	3	C_6
12,800 Gy	1	3	3	1	3	C_6

Table 4
Area (or spectral irradiance, $W/m^2/nm$) of each transition in the $RE_2Hf_2O_7:Eu^{3+}$ (RE = Y, La, Gd, and Lu) NCs and corresponding asymmetric ratio.

	$^5D_0 \rightarrow {}^7F_0$	$^5D_0 \rightarrow {}^7F_1$	$^5D_0 \rightarrow {}^7F_2$	$^5D_0 \rightarrow {}^7F_3$	$^5D_0 \rightarrow {}^7F_4$	Asymmetry ratio
$Y_2Hf_2O_7:Eu^{3+}$						
Unexposed	3.14E7	2.49E8	7.20E8	1.31E8	2.55E8	**2.89**
800 Gy	1.89E7	1.87E8	4.65E8	8.13E7	1.62E8	**2.49**
3200 Gy	2.33E7	1.86E8	5.44E8	9.52E7	1.86E8	**2.92**
12,800 Gy	2.31E7	2.49E8	5.49E8	9.68E7	1.938	**2.20**
$La_2Hf_2O_7:Eu^{3+}$						
Unexposed	1.36E8	9.91E8	2.84E9	3.99E8	9.06E8	**2.86**
800 Gy	6.92E7	4.95E8	1.42E9	2.23E8	4.72E8	**2.87**
3200 Gy	4.74E7	2.51E8	9.19E8	1.25E8	2.97E8	**3.67**
12,800 Gy	8.21E7	5.14E8	1.48E9	2.19E8	4.95E8	**2.88**
$Gd_2Hf_2O_7:Eu^{3+}$						
Unexposed	1.16E7	8.66E7	2.73E8	4.221E7	8.40E7	**3.15**
800 Gy	3.23E7	2.28E8	6.70E8	1.14E8	2.44E8	**2.94**
3200 Gy	2.72E7	1.90E8	5.79E8	9.62E7	2.14E8	**3.04**
12,800 Gy	2.51E7	1.73E8	5.53E8	9.09E7	2.07E8	**3.19**
$Lu_2Hf_2O_7:Eu^{3+}$						
Unexposed	1.57E6	1.63E7	4.29E7	7.96E6	1.77E7	**2.62**
800 Gy	1.33E6	1.06E7	3.10E7	4.76E6	1.24E7	**2.92**
3200 Gy	3.40E6	3.48E7	9.28E7	1.66E7	3.27E7	**2.67**
12,800 Gy	1.25E6	1.32E7	3.49E7	6.51E6	1.40E7	**2.64**

indicated that the symmetry around Eu^{3+} ions is very low [63,70,71]. In all four $RE_2Hf_2O_7$:5%Eu^{3+} (RE = Y, La, Gd, and Lu) samples, a very weak peak was observed around 740–760 nm, which is not often seen but could be attributed to the $^5D_0 \rightarrow {}^7F_5$ transition of the Eu^{3+} ion [72].

In all of these emission spectra, three important observations can be made: (i) the presence of the $^5D_0 \rightarrow {}^7F_0$ transition, which is neither allowed by the MDT nor by EDT, (ii) Spectral features exhibit high extent of stark splitting in all the europium doped samples, and (iii) higher intensity of EDT than MDT. These three observations are the typical features of Eu^{3+} ions localized in highly asymmetric and distorted environment. In fact, the $^5D_0 \rightarrow {}^7F_0$ transition is only allowed when the symmetry around europium is $\leq C_{nv}/C_n$ and C_s. According to the electric dipole selection rule, this transition is normally seen in the following 10 point group symmetries: C_s, C_1, C_2, C_3, C_4, C_6, C_{2V}, C_{3V}, C_{4V}, and C_{6V} [71]. Table 3 tabulates the point groups and stark splitting component in our $RE_2Hf_2O_7:Eu^{3+}$ (RE = Y, La, Gd, and Lu) NCs before and after γ-ray exposure based on previous reports on NCs [72,73]. Specifically, the $Y_2Hf_2O_7:Eu^{3+}$ sample displayed point group symmetry of C_{4v} both before and after exposure to γ-ray irradiation. This suggested that γ-ray irradiation did not disturb the local environment of the Eu^{3+} ion in the $Y_2Hf_2O_7$ host. The $La_2Hf_2O_7:Eu^{3+}$ sample displayed a lower point group symmetry of C_{3v} before exposure to γ-rays compared to the $Y_2Hf_2O_7:Eu^{3+}$ sample with C_{4v} symmetry. After γ-ray exposure with different doses, the point group symmetry of the Eu^{3+} ion in $La_2Hf_2O_7$ changed to C_{6v} after the γ-ray exposure to 800 Gy, then to C_6 after the γ-ray exposure to 3,200 Gy and to 12,800 Gy. This may be due to the γ-ray radiation disrupting the local symmetry around Eu^{3+} at the La^{3+}/Hf^{4+} sites. On the contrary, for the $Gd_2Hf_2O_7:Eu^{3+}$ and $Lu_2Hf_2O_7:Eu^{3+}$ NCs, the point group symmetry around the Eu^{3+} ions remained C_6 under all the studied conditions.

Therefore, other than the $La_2Hf_2O_7:Eu^{3+}$ sample, it appears that γ-ray irradiation does not induce many changes in the local symmetry of the Eu^{3+} ion in our $RE_2Hf_2O_7:Eu^{3+}$ (RE = Y, Gd, and Lu) NCs. This pattern may be due to the difference of the RE-O bond lengths. The RE-O bond length is largest in La-O compared to the other RE-O bonds with the following decreasing order: La-O > Gd-O > Y-O > Lu-O. Consequently, the La-O bond is the weakest among the four, which makes it more susceptible to changes – including breaking – caused by the γ-ray irradiation compared to the other RE-O bonds. It is also worth mentioning that the ionic radius of Eu^{3+} is most similar to that of La^{3+} and the least similar to that of Lu^{3+}. This difference in the ionic radii of the Eu^{3+} ion and the RE ion may cause the point group symmetry of the

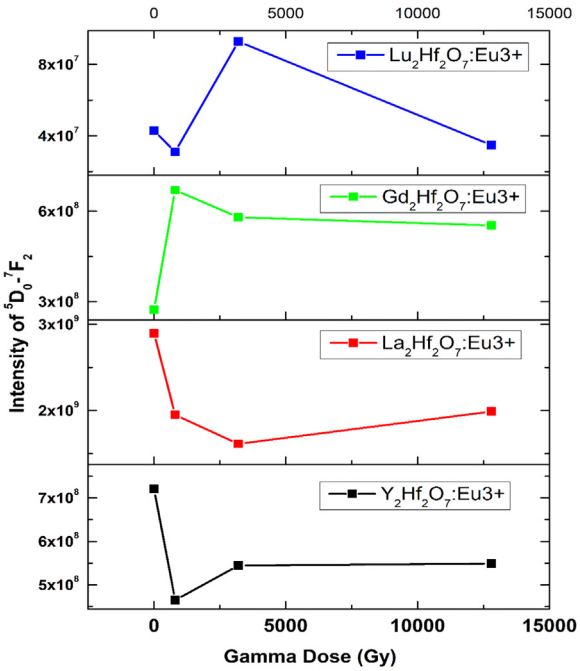

Fig. 6. Effect of γ-ray doses on the PL emission intensity of Eu^{3+} doped $Y_2Hf_2O_7$, $La_2Hf_2O_7$, $Gd_2Hf_2O_7$ and $Lu_2Hf_2O_7$.

Eu^{3+} ion to differ among the $RE_2Hf_2O_7$:Eu^{3+} NCs with different RE^{3+} species. In an ideal pyrochlore structure, the A and B sites have D_{3d} symmetry, which demands only the MDT to be seen in the Eu^{3+} emission spectrum with only 2 stark splitting components. This simple pattern was not observed from the $RE_2Hf_2O_7$:Eu^{3+} samples under our experimental conditions. After doping, the Eu^{3+} ions may have been distributed at either the RE^{3+} ionic site or the Hf^{4+} site. This may be the cause of the decrease in the symmetry of the La^{3+} RE site from D_{3d} in all of our $RE_2Hf_2O_7$:Eu^{3+} samples. The ionic radii of 8 and 6-coordinated Eu^{3+} ions are 107 and 95 pm, respectively. In general, the Eu^{3+} ion is much closer in size to the RE^{3+} ions and will be much more likely to occupy the RE^{3+} site compared to the much smaller Hf^{4+} site. Correspondingly, the ionic charge difference between Hf^{4+} and Eu^{3+} allows little distortion of the lattice due to the need for charge compensated oxygen vacancies. If the associated charge compensating defects arise due to a large charge/size mismatch, the local site symmetry around the Eu^{3+} occupying the RE^{3+} site will have a center of inversion with some Eu^{3+} ions also occupying the Hf^{4+} site without inversion symmetry. This will cause a high asymmetry value (Table 4) in all of our $RE_2Hf_2O_7$:Eu^{3+} NCs. Table 4 also depicts the area under the curve for all the major transitions of the $RE_2Hf_2O_7$:Eu^{3+} (RE = Y, La, Gd, and Lu) samples.

The intensity of the hypersensitive EDT plotted as a function of γ-ray irradiation dose is depicted in Fig. 6. Different trends were seen from these $RE_2Hf_2O_7$:Eu^{3+} (RE = Y, La, and Gd) NCs. With increasing γ-ray irradiation doses, the $Y_2Hf_2O_7$:Eu^{3+} and $La_2Hf_2O_7$:Eu^{3+} samples experienced a decrease in PL output while the $Gd_2Hf_2O_7$:Eu^{3+} sample experienced an increase in PL output. For the $Lu_2Hf_2O_7$:Eu^{3+} sample, there was a marginal decrease in PL emission intensity at very low (800 Gy) and very high (12,800 Gy) γ-ray doses, but there was a significant enhancement after the γ-ray exposure to 3200 Gy. The PL emission intensity decrease seen from the $Y_2Hf_2O_7$:Eu^{3+} and $La_2Hf_2O_7$:Eu^{3+} samples with increasing γ-ray irradiation may be caused

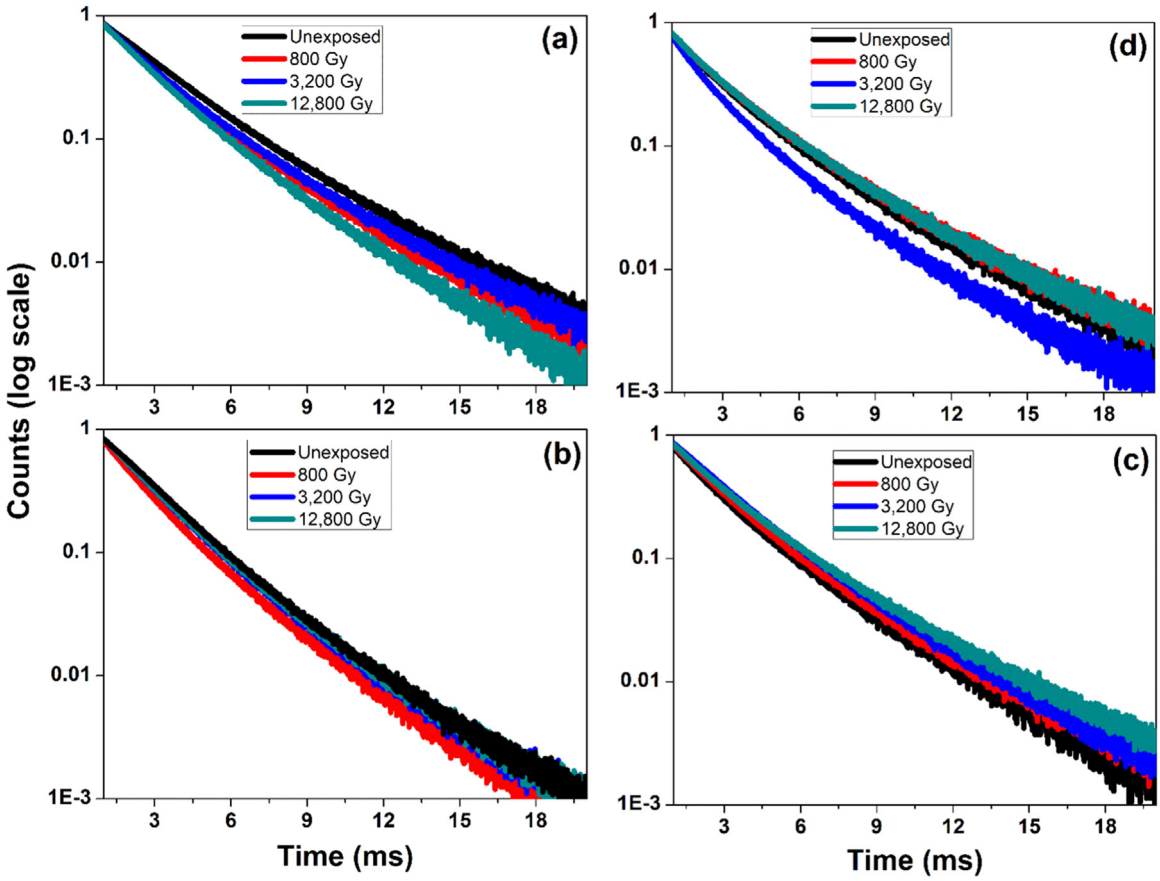

Fig. 7. PL decay curves of the Eu^{3+} doped (a) $Y_2Hf_2O_7$, (b) $La_2Hf_2O_7$, (c) $Gd_2Hf_2O_7$, and (d) $Lu_2Hf_2O_7$ NCs before and after γ-ray irradiation with doses of 800, 3200 and 12,800 Gy (Gy).

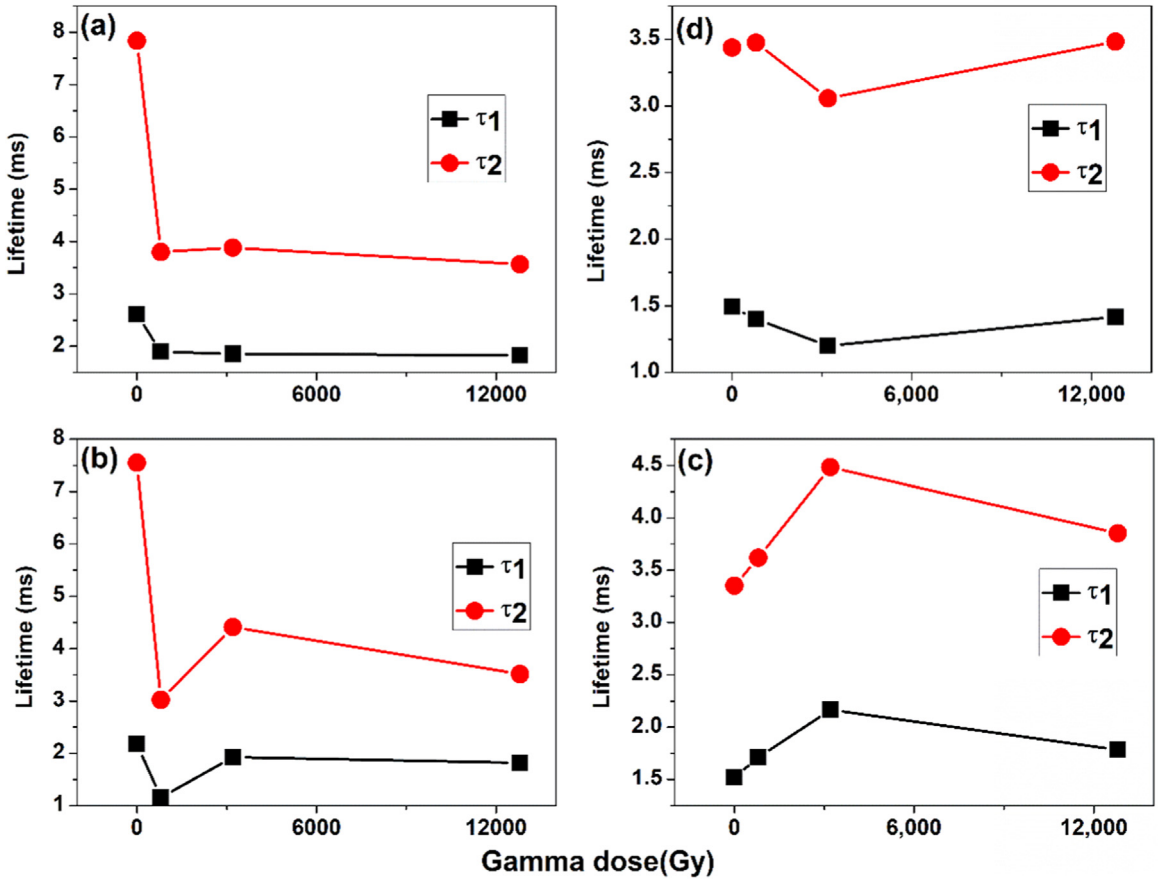

Fig. 8. τ_1 and τ_2 lifetime values as function of γ-ray dose: (a) $Y_2Hf_2O_7:Eu^{3+}$, (b) $La_2Hf_2O_7:Eu^{3+}$, (c) $Gd_2Hf_2O_7:Eu^{3+}$, and (d) $Lu_2Hf_2O_7:Eu^{3+}$ NCs.

by the interaction of the γ-ray with atomic nuclei or electrons. It is expected that highly energetic γ-ray radiation will interact strongly with its atomic nuclei or electrons. Such interactions lead to scattering of particles (elastic as well as inelastic) followed by atomic excitation and ionization, nuclear reactions, and structural perturbation. All these γ-ray-induced changes cause radiation damage [74]. After γ-ray exposure, many defects are created in the lattice such as point defects, defect cluster, columnar defects etc [75]. These defects aid in non-radiative transitions (cation vacancies, surface defects) by providing additional pathways and thus reduced the emission intensity [25]. On the contrary, for the $Gd_2Hf_2O_7:Eu^{3+}$ sample, γ-ray irradiation led to an enhancement in PL emission intensity. In this case, the concentration of oxygen defects is much more than those of cation vacancies, surface defects, or defect clusters. This led to an intense host emission [47,76], and therefore a highly efficient host-dopant energy transfer took place. This ultimately led to an increased Eu^{3+} PL emission in the $Gd_2Hf_2O_7:Eu^{3+}$ sample. For the $Lu_2Hf_2O_7:Eu^{3+}$ sample, after the γ-ray exposure to low (800 Gy) and high (12,800 Gy) doses, more surface defects, cation vacancies, and defects cluster were seen whereas the intermediate γ-ray dose of 3200 Gy led to more oxygen defects. This explains the unusual behavior of the $Lu_2Hf_2O_7:Eu^{3+}$ sample after being exposed to different γ-ray doses.

As in the XRD and Raman data shown previously (Figs. 1 and 2), a similar trend can be seen once again in the peak shifting of the emission spectra of the $La_2Hf_2O_7:Eu^{3+}$ and $Lu_2Hf_2O_7:Eu^{3+}$ samples. The $La_2Hf_2O_7:Eu^{3+}$ sample experienced a red-shift of the $^5D_0 \rightarrow {}^7F_1$ and $^5D_0 \rightarrow {}^7F_2$ transition peaks after the γ-ray exposure to 3200 Gy. The $Lu_2Hf_2O_7:Eu^{3+}$ sample also experienced similar red-shift of the $^5D_0 \rightarrow {}^7F_2$ transition as well as a typical splitting of the $^5D_0 \rightarrow {}^7F_1$ transition peak after the γ-ray exposure to 800 Gy. The spectral shift and change of relative intensity of the $^5D_0 \rightarrow {}^7F_1$ and $^5D_0 \rightarrow {}^7F_2$ transitions after the γ-ray exposure experienced from the $La_2Hf_2O_7:Eu^{3+}$ and $Lu_2Hf_2O_7:Eu^{3+}$ samples indicates a possible change in the local host environment of the Eu^{3+} ions after the γ-ray exposure to 800 and 3200 Gy. The $Y_2Hf_2O_7:Eu^{3+}$ and $Gd_2Hf_2O_7:Eu^{3+}$ samples did not experience observable peak shift throughout the γ-ray irradiation process.

Fig. 7 depicts the luminescence decay profiles of the $Y_2Hf_2O_7:Eu^{3+}$, $La_2Hf_2O_7:Eu^{3+}$, $Gd_2Hf_2O_7:Eu^{3+}$, and $Lu_2Hf_2O_7:Eu^{3+}$ NCs before and after γ-ray irradiation with doses of 800, 3200 and 12800 Gy (Gy). All the samples displayed biexponential decay behavior typical of Eu^{3+} distribution at multiple sites in $A_2B_2O_7$ type matrix sitting at both A and B site. The PL decay curves were fitted via a multi-exponential decay function [65]: $I(t) = A_1 e^{\left(-\frac{t}{\tau 1}\right)} + A_2 e^{\left(-\frac{t}{\tau 2}\right)}$, where τ_1 and τ_2 are the short and long components of the decay lifetime curve and A_1 and A_2 are fitting parameters. In line with the emission data, the lifetime values were also found to be decrease after γ-ray exposure for $Y_2Hf_2O_7:Eu^{3+}$ and $La_2Hf_2O_7:Eu^{3+}$ samples and increase for $Gd_2Hf_2O_7:Eu^{3+}$ and $Lu_2Hf_2O_7:Eu^{3+}$ sample. This can be attributed to large concentration of defects (including surface defects, defect clusters, cation vacancies etc.) formed by gamma-ray irradiation in the case of rare earth hafnates of rare earth ions with no f-electrons. These defects provide additional pathways for non-radiative decay as a results of lifetime decreases. For systems with a half shell or full shell of f-configurations such as f^7 of Gd^{3+} ions or f^{14} of Lu^{3+} ions, gamma-ray irradiation generated oxygen vacancies which act as recombination centers, which combine photo-excited holes and thereby aid in radiative transition and increases in the lifetime. Based on the concept of phonon energy the f-f transition is forbidden for symmetric europium sites whereas it is allowed for transitions taking place from assymmetric europium sites [63,77–82]. In this case, the RE^{3+} sites have a more symmetric scalenohedra environment whereas Hf^{4+} sites have a low symmetry octahedra. Eu^{3+} ions occupying REO_8 site will have inversion symmetry or a more

symmetric structure compared to those occupying HfO_6 site. The short lifetime values in the range of 1.5–3.5 ms are attributed to asymmetric site and arises when the Eu^{3+} ions are localized in the distorted HfO_6 octahedra. On the other hand, the long lifetime values in the range of 3.5–7.8 ms are attributed to the symmetric REO_8 scalenohedra. The chi-square values for the biexponential fitting fall in between 0.93 and 1.12. Fig. 8 depicts the change in τ_1 and τ_2 values as the γ-ray irradiation dose increases. Both lifetime values displayed similar trends as a function of the γ-ray dose.

4. Conclusion

Europium doped rare earth hafnate $RE_2Hf_2O_7:Eu^{3+}$ (RE = Y, La, Pr, Gd, Er, Lu) nanocrystalline samples were exposed to varying γ-ray doses, and analyzed for changes in crystal structural and optical properties. Structural analysis revealed $Y_2Hf_2O_7:Eu^{3+}$ and $Gd_2Hf_2O_7:Eu^{3+}$ samples retained their crystal structures exhibiting robust chemical stability without experiencing changes even after the highest γ-ray exposure to 12,800 Gy, the $Pr_2Hf_2O_7:Eu^{3+}$ and $Er_2Hf_2O_7:Eu^{3+}$ samples were also seen to be stable under all γ-ray doses, while the $La_2Hf_2O_7:Eu^{3+}$ and $Lu_2Hf_2O_7:Eu^{3+}$ samples were not as stable as the others showing a possible order-disordered phase transformation after exposure to 800 and 3200 Gy. The luminescence output of the $La_2Hf_2O_7:Eu^{3+}$ and $Y_2Hf_2O_7:Eu^{3+}$ samples underwent considerable radiation damage after γ-ray irradiation due to a large concentration of cation vacancies, surface defects and defect clusters which caused a decrease in fluorescence intensity. On the contrary, the $Gd_2Hf_2O_7:Eu^{3+}$ sample displayed a prominent enhancement in luminescence output after γ-ray exposure – attributed to increased oxygen vacancies compared to other emission quenching defects. Furthermore, a similar trend can be seen in the lifetime measurements. $Lu_2Hf_2O_7:Eu^{3+}$ appeared to display some abnormal optical properties by undergoing PL reduction after the lowest (800 Gy) and highest (12,800 Gy) γ-ray doses, but experiencing an increase after the median dose (3200 Gy). More studies on the effects of γ-ray radiation on the order-disorder phase transformation of these compositions is needed to fully understand the chemical processes. In conclusion, the best potential candidates for the HLW use were determined to be $RE_2Hf_2O_7$ (RE = Y, Pr, Gd, and Er). $La_2Hf_2O_7:Eu^{3+}$ and $Lu_2Hf_2O_7:Eu^{3+}$ are good candidates for future studies on how various radiations affect the order-disorder phase transformation in different $A_2B_2O_7$ compositions and their chemical stability.

Acknowledgment

The authors thank the financial support by the National Science Foundation USA under CHE (award #1710160) and DMR (grant #1523577) and the USDA National Institute of Food and Agriculture USA (award #2015-38422-24059,). The Department of Chemistry at the University of Texas Rio Grande Valley is grateful for the generous support provided by a Departmental Grant from the Robert A. Welch Foundation USA (Grant No. BX-0048). SKG thanks the United States-India Education Foundation (USIEF) and the Institute of International Education (IIE) for his Fulbright Nehru Postdoctoral Fellowship India (Award# 2268/FNPDR/2017).

References

[1] M.C.M. Angub, C.J.T. Vergara, H.A.F. Husay, A.A. Salvador, M.J.F. Empizo, K. Kawano, Y. Minami, T. Shimizu, N. Sarukura, A.S. Somintac, Hydrothermal growth of vertically aligned ZnO nanorods as potential scintillator materials for radiation detectors, J. Lumin. 203 (2018) 427–435.
[2] T. Maheswari, C. Basavapoornima, K. Linganna, S. Ju, W.T. Han, C.K. Jayasankar, Structural and spectroscopic properties of γ-ray irradiated Er3+-doped lead phosphate glasses, J. Lumin. 203 (2018) 322–330.
[3] T. Ogawa, D. Nakauchi, G. Okada, N. Kawaguchi, T. Yanagida, Photoluminescence and scintillation properties of Ce-doped Sr2Al2SiO7 crystals, J. Lumin. 202 (2018) 409–413.
[4] S. Tamboli, R.M. Kadam, B. Rajeswari, B. Singh, S.J. Dhoble, Correlated PL, TL and EPR study in γ-rays and C6+ ion beam irradiated CaMg2(SO4)3:Dy3+ triple sulphate phosphor, J. Lumin. 203 (2018) 267–276.
[5] D. Sporea, L. Mihai, D. Neguţ, Y. Luo, B. Yan, M. Ding, S. Wei, G.-D. Peng, γ irradiation induced effects on bismuth active centres and related photoluminescence properties of Bi/Er co-doped optical fibres, Sci. Rep. 6 (2016) 29827.
[6] G. Gaur, D.S. Koktysh, D.M. Fleetwood, R.A. Weller, R.A. Reed, B.R. Rogers, S.M. Weiss, Influence of ionizing radiation and the role of thiol ligands on the reversible photodarkening of CdTe/CdS quantum dots, ACS Appl. Mater. Interfaces 8 (2016) 7869–7876.
[7] S.P. Jovanovic, Z. Syrgiannis, Z.M. Markovic, A. Bonasera, D.P. Kepic, M.D. Budimir, Da.D. Milivojević, V.D. Spasojevic, M.D. Dramićanin, V.B. Pavlovic, Modification of structural and luminescence properties of graphene quantum dots by gamma irradiation and their application in a photodynamic therapy, ACS Appl. Mater. Interfaces 7 (2015) 25865–25874.
[8] T. Wang, C.J. Reckmeier, S. Lu, Y. Li, Y. Cheng, F. Liao, A.L. Rogach, M. Shao, Gamma ray shifted and enhanced photoluminescence of graphene quantum dots, J. Mater. Chem. C 4 (2016) 10538–10544.
[9] N. Lavanya, C. Sekar, A. Anithaa, N. Sudhan, K. Asokan, A. Bonavita, S. Leonardi, G. Neri, Investigations on the effect of gamma-ray irradiation on the gas sensing properties of SnO_2 nanoparticles, Nanotechnology 27 (2016) 385502.
[10] S. Ranwa, S.S. Barala, M. Fanetti, M. Kumar, Effect of gamma irradiation on Schottky-contacted vertically aligned ZnO nanorod-based hydrogen sensor, Nanotechnology 27 (2016) 345502.
[11] M.H. Hasim, I. Abdul Rahman, S. Rahim, M.T.M. Ayob, S. Sharin, S. Radiman, Study on the effect of γ-irradiation on gadolinium oxysulfide nanophosphors (Gd_2O_2S-NPs), J. Nanomater. 2017 (2017).
[12] M. Elistratova, N. Romanov, D. Goryachev, I. Zakharova, O. Sreseli, Effect of gamma irradiation on the photoluminescence of porous silicon, Semiconductors 51 (2017) 483–487.
[13] S. Sadhasivam, N. Rajesh, Structural and optical effects induced by gamma irradiation on $NdPO_4$: X-ray diffraction, spectroscopic and luminescence study, Mater. Res. Bull. 74 (2016) 117–123.
[14] B.H. Babu, V.R.K. Kumar, Warm white light generation in γ-irradiated Dy^{3+}, Eu^{3+} codoped sodium aluminoborate glasses, J. Lumin. 169 (2016) 16–23.
[15] P. Mahadik, P. Sengupta, B. Vishwanadh, S. Mishra, V. Sudarsan, G. Dey, Effect of γ-irradiation on structure and properties of Nd^{3+} doped perovskite, Radiat. Phys. Chem. 139 (2017) 152–156.
[16] J. Zhang, H. Riesen, Controlled generation of Tm^{2+} Ions in nanocrystalline $BaFCl:Tm^{3+}$ by X-ray irradiation, J. Phys. Chem. A 121 (2017) 803–809.
[17] M. Subramanian, G. Aravamudan, G.S. Rao, Oxide pyrochlores—a review, Prog. Solid State Chem. 15 (1983) 55–143.
[18] S. Zhang, H. Zhang, F. Zhao, M. Jiang, H. Xiao, Z. Liu, X. Zu, Impact of isovalent and aliovalent substitution on the mechanical and thermal properties of $Gd_2Zr_2O_7$, Sci. Rep. 7 (2017) 6399.
[19] J.P. Zuniga, S.K. Gupta, M. Abdou, Y. Mao, Effect of molten salt synthesis processing duration on the photo- and radioluminescence of UV-, visible-, and X-ray-excitable $Gd_2Hf_2O_7:Eu^{3+}$ nanoparticles, ACS Omega 3 (7) (2018) 7757–7770.
[20] J.P. Zuniga, S.K. Gupta, M. Pokhrel, Y. Mao, Exploring the optical properties of $La_2Hf_2O_7:Pr^{3+}$ nanoparticles under UV and X-ray excitation for potential lighting and scintillating applications, New J. Chem. 42 (12) (2018) 9381–9392.
[21] B.P. Uberuaga, M. Tang, C. Jiang, J.A. Valdez, R. Smith, Y. Wang, K.E. Sickafus, Opposite correlations between cation disordering and amorphization resistance in spinels versus pyrochlores, Nat. Commun. 6 (2015) 8750.
[22] J. Park, M. Park, G. Nam, M.G. Kim, J. Cho, Unveiling the catalytic origin of nanocrystalline yttrium ruthenate pyrochlore as a bifunctional electrocatalyst for Zn–Air batteries, Nano Lett. 17 (2017) 3974–3981.
[23] X. Yin, X. Li, W. Gu, F. Wang, Y. Zou, S. Sun, Z. Fu, Y. Lu, Enhanced photocatalytic activities of g-C_3N_4 via hybridization with a Bi–Fe–Nb-containing ferroelectric pyrochlore, ACS Appl. Mater. Interfaces 9 (2017) 19908–19916.
[24] E. Kermarrec, J. Gaudet, K. Fritsch, R. Khasanov, Z. Guguchia, C. Ritter, K. Ross, H. Dabkowska, B. Gaulin, Ground state selection under pressure in the quantum pyrochlore magnet $Yb_2Ti_2O_7$, Nat. Commun. 8 (2017) 14810.
[25] S.K. Gupta, K. Sudarshan, P. Ghosh, A. Srivastava, S. Bevara, P. Pujari, R. Kadam, Role of various defects in the photoluminescence characteristics of nanocrystalline $Nd_2Zr_2O_7$: an investigation through spectroscopic and DFT calculations, J. Mater. Chem. C 4 (2016) 4988–5000.
[26] M. Pokhrel, A. Burger, M. Groza, Y. Mao, Enhance the photoluminescence and radioluminescence of $La_2Zr_2O_7$: Eu^{3+} core nanoparticles by coating with a thin Y_2O_3 shell, Opt. Mater. 68 (2017) 35–41.
[27] M. Abdou, S.K. Gupta, J.P. Zuniga, Y. Mao, On structure and phase transformation of uranium doped $La_2Hf_2O_7$ nanoparticles as an efficient nuclear waste host, Mater. Chem. Front. (2018).
[28] Y.H. Li, Y.Q. Wang, C.P. Xu, J.A. Valdez, M. Tang, K.E. Sickafus, Microstructural evolution of the pyrochlore compound $Er_2Ti_2O_7$ induced by light ion irradiations, Nucl. Instrum. Methods Phys. Res. Sect. B: Beam Interact. Mater. At. 286 (2012) 218–222.
[29] D.Y. Yang, C.P. Xu, E.G. Fu, J. Wen, C.G. Liu, K.Q. Zhang, Y.Q. Wang, Y.H. Li, Structure and radiation effect of Er-stuffed pyrochlore $Er_2(Ti_{2-x}Er_x)O_{7-x/2}$ (x = 0–0.667), Nucl. Instrum. Methods Phys. Res. Sect. B: Beam Interact. Mater. At. 357 (2015) 69–74.
[30] J. Shamblin, C.L. Tracy, R.C. Ewing, F. Zhang, W. Li, C. Trautmann, M. Lang, Structural response of titanate pyrochlores to swift heavy ion irradiation, Acta Mater. 117 (2016) 207–215.
[31] D. Yang, Y. Xia, J. Wen, J. Liang, P. Mu, Z. Wang, Y. Li, Y. Wang, Role of ion species in radiation effects of $Lu_2Ti_2O_7$ pyrochlore, J. Alloy. Compd. 693 (2017) 565–572.

[32] S.L. Weeden-Wright, S.L. Gollub, R. Harl, A.B. Hmelo, D.M. Fleetwood, B.R. Rogers, R.D. Schrimpf, D.G. Walker, Radiation effects on the photoluminescence of rare-earth doped pyrochlore powders, IEEE Trans. Nucl. Sci. 60 (2013) 2444–2449.

[33] J. Lian, R.C. Ewing, L.M. Wang, K.B. Helean, Ion-beam irradiation of $Gd_2Sn_2O_7$ and $Gd_2Hf_2O_7$ pyrochlore: bond-type effect, J. Mater. Res. 19 (2011) 1575–1580.

[34] Y.H. Li, J. Wen, Y.Q. Wang, Z.G. Wang, M. Tang, J.A. Valdez, K.E. Sickafus, The irradiation effects of $Gd_2Hf_2O_7$ and $Gd_2Ti_2O_7$, Nucl. Instrum. Methods Phys. Res. Sect. B: Beam Interact. Mater. At. 287 (2012) 130–134.

[35] F. Lu, Y. Shen, Z. Dong, G. Wang, F. Zhang, R.C. Ewing, J. Lian, Ion beam irradiation-induced amorphization of nano-sized $K_xLn_yTa_2O_{7-v}$ tantalate pyrochlore, Front. Energy Res. 2 (2014).

[36] K.E. Sickafus, L. Minervini, R.W. Grimes, J.A. Valdez, M. Ishimaru, F. Li, K.J. McClellan, T. Hartmann, Radiation tolerance of complex oxides, Science 289 (2000) 748–751.

[37] C.L. Tracy, J. Shamblin, S. Park, F. Zhang, C. Trautmann, M. Lang, R.C. Ewing, Role of composition, bond covalency, and short-range order in the disordering of stannate pyrochlores by swift heavy ion irradiation, Phys. Rev. B 94 (2016) 064102.

[38] Y. Xia, C.G. Liu, D.Y. Yang, J. Wen, H. Liu, P.C. Mu, Y.H. Li, Synthesis and radiation tolerance of $Lu_{2-x}Ce_xTi_2O_7$ pyrochlores, J. Nucl. Mater. 480 (2016) 182–188.

[39] A. Soulié, D. Menut, J.-P. Crocombette, A. Chartier, N. Sellami, G. Sattonnay, I. Monnet, J.-L. Béchade, X-ray diffraction study of the $Y_2Ti_2O_7$ pyrochlore disordering sequence under irradiation, J. Nucl. Mater. 480 (2016) 314–322.

[40] W.M. R, C.D. R, Oxide materials with low thermal conductivity, J. Am. Ceram. Soc. 90 (2) (2007) 533–540.

[41] M. Abdou, S.K. Gupta, J.P. Zuniga, Y. Mao, On structure and phase transformation of uranium doped $La_2Hf_2O_7$ nanoparticles as an efficient nuclear waste host, Mater. Chem. Front. (2018).

[42] V.A. Vorozhtcov, V.L. Stolyarova, S.I. Lopatin, E.P. Simonenko, N.P. Simonenko, K.A. Sakharov, V.G. Sevastyanov, N.T. Kuznetsov, Vaporization and thermodynamic properties of lanthanum hafnate, J. Alloy. Compd. 735 (2018) 2348–2355.

[43] S.K. Gupta, J.P. Zuniga, M. Abdou, Y. Mao, Thermal annealing effects on $La_2Hf_2O_7$:Eu^{3+} nanoparticles: a curious case study of structural evolution and site-specific photo- and radio-luminescence, Inorg. Chem. Front. (2018).

[44] V.G. Toporova, V.V. Pimenov, V.D. Risovanyi, A.V. Zakharov, Results of SM reactor tests of dysprosium hafnate, At. Energy 110 (2011) 259.

[45] Y. Mao, X. Guo, J.Y. Huang, K.L. Wang, J.P. Chang, Luminescent nanocrystals with $A_2B_2O_7$ composition synthesized by a kinetically modified molten salt method, J. Phys. Chem. C 113 (2009) 1204–1208.

[46] J.P. Zuniga, M. Abdou, S.K. Gupta, Y. Mao, Molten-Salt Synthesis of Complex Metal Oxide Nanoparticles, JoVE e58482.

[47] S.K. Gupta, J.P. Zuniga, P.S. Ghosh, M. Abdou, Y. Mao, Correlating structure and luminescence properties of undoped and $La_2Hf_2O_7$:Eu^{3+} NPs prepared with different coprecipitating pH values through experimental and theoretical studies, Inorg. Chem. (2018).

[48] J.P. Zuniga, S.K. Gupta, M. Abdou, Y. Mao, Effect of molten salt synthesis processing duration on the photo- and radioluminescence of UV-, Visible-, and X-ray-excitable $La_2Hf_2O_7$:Eu^{3+} nanoparticles, ACS Omega 3 (2018) 7757–7770.

[49] K. Wahid, M. Pokhrel, Y. Mao, Structural, photoluminescence and radioluminescence properties of Eu^{3+} doped $La_2Hf_2O_7$ nanoparticles, J. Solid State Chem. 245 (2017) 89–97.

[50] W.-H. Wang, K.L.I. Matthews, R.E. Teague, Dose rates from a cobalt-60 pool irradiator measured with fricke dosimeters, Health Phys. 94 (2008) S44–S50.

[51] C. Narula, R.P. Chauhan, High dose gamma ray exposure effect on the properties of CdSe nanowires, Radiat. Phys. Chem. 144 (2018) 405–412.

[52] N. Okasha, S.I. El Dek, M.K. Abdelmaksoud, D.N. Ghaffar, Enhanced structure and magnetic properties of doped nanomagnetite by γ-irradiation, J. Alloy. Compd. 737 (2018) 356–364.

[53] F.N. Sayed, V. Grover, K. Bhattacharyya, D. Jain, A. Arya, C.G.S. Pillai, A.K. Tyagi, $Sm_{2-x}Dy_xZr_2O_7$ pyrochlores: probing order − disorder dynamics and multifunctionality, Inorg. Chem. 50 (2011) 2354–2365.

[54] M.T. Katlyn, R.R. Dylan, A.H. Rachel, L.T. Cameron, L.T. Madison, F.F. Antonio, L.M. Wendy, C.E. Rodney, Pressure-induced structural modifications of rare-earth hafnate pyrochlore, J. Phys.: Condens. Matter 29 (2017) 255401.

[55] T.M.H. Nguyen, L.J. Sandilands, C.H. Sohn, C.H. Kim, A.L. Wysocki, I.-S. Yang, S.J. Moon, J.-H. Ko, J. Yamaura, Z. Hiroi, T.W. Noh, Two-magnon scattering in the 5d all-in-all-out pyrochlore magnet $Cd_2Os_2O_7$, Nat. Commun. 8 (2017) 251.

[56] V.V. Popov, A.P. Menushenkov, B.R. Gaynanov, V.Z. Ya, R.D. Svetogorov, A.A. Yastrebtsev, A.A. Pisarev, L.A. Arzhatkina, K.V. Ponkratov, Features of formation and evolution of crystal and local structures in nanocrystalline Ln 2 Zr 2 O 7 (Ln = La - Tb), J. Phys.: Conf. Ser. 941 (1) (2017) 012079.

[57] C.R. Stanek, C. Jiang, B.P. Uberuaga, K.E. Sickafus, A.R. Cleave, R.W. Grimes, Predicted structure and stability of $A_4B_3O_{12-\delta}$ -phase compositions, Phys. Rev. B 80 (17) (2009) 174101.

[58] B.P. Mandal, N. Garg, S.M. Sharma, A.K. Tyagi, Preparation, XRD and Raman spectroscopic studies on new compounds $RE_2Hf_2O_7$ (RE = Dy, Ho, Er, Tm, Lu, Y): pyrochlores or defect-fluorite? J. Solid State Chem. 179 (7) (2006) 1990–1994.

[59] S.C. R, G.R. W, Prediction of rare-earth $A_2Hf_2O_7$ pyrochlore phases, J. Am. Ceram. Soc. 85 (2002) 2139–2141.

[60] M. Lang, F. Zhang, J. Zhang, J. Wang, J. Lian, W.J. Weber, B. Schuster, C. Trautmann, R. Neumann, R.C. Ewing, Review of $A_2B_2O_7$ pyrochlore response to irradiation and pressure, Nucl. Instrum. Methods Phys. Res. Sect. B: Beam Interact. Mater. At. 268 (19) (2010) 2951–2959.

[61] F.X. Zhang, J.W. Wang, J. Lian, M.K. Lang, U. Becker, R.C. Ewing, Phase stability and pressure dependence of defect formation in $Gd_2Ti_2O_7$ and $Gd_2Sn_2O_7$ pyrochlores, Phys. Rev. Lett. 100 (2008) 045503.

[62] S.K. Gupta, P.S. Ghosh, A.K. Yadav, S.N. Jha, D. Bhattacharyya, R.M. Kadam, Origin of blue-green emission in α-$Zn_2P_2O_7$ and local structure of Ln^{3+} Ion in α-$Zn_2P_2O_7$:Ln^{3+} (Ln = Sm, Eu): time-resolved photoluminescence, EXAFS, and DFT measurements, Inorg. Chem. 56 (2017) 167–178.

[63] S.K. Gupta, C. Reghukumar, R. Kadam, Eu^{3+} local site analysis and emission characteristics of novel $Nd_2Zr_2O_7$:Eu phosphor: insight into the effect of europium concentration on its photoluminescence properties, RSC Adv. 6 (2016) 53614–53624.

[64] S.K. Gupta, P. Ghosh, C. Reghukumar, N. Pathak, R. Kadam, Experimental and theoretical approach to account for green luminescence from $Gd_2Zr_2O_7$ pyrochlore: exploring the site occupancy and origin of host-dopant energy transfer in $Gd_2Zr_2O_7$:Eu^{3+}, RSC Adv. 6 (2016) 44908–44920.

[65] M. Pokhrel, K. Wahid, Y. Mao, Systematic studies on $RE_2Hf_2O_7$: 5% Eu^{3+} (RE = Y, La, Pr, Gd, Er, and Lu) nanoparticles: effects of the A-site RE^{3+} cation and calcination on structure and photoluminescence, J. Phys. Chem. C 120 (2016) 14828–14839.

[66] X.T. Zu, N. Li, F. Gao, First-principles study of structural and energetic properties of $A_2Hf_2O_7$ (A = Dy, Ho, Er) compounds, J. Appl. Phys. 104 (2008) 043517.

[67] G. Blasse, On the Eu^{3+} fluorescence of mixed metal oxides. IV. The photoluminescent efficiency of Eu^{3+}-activated oxides, J. Chem. Phys. 45 (1966) 2356–2360.

[68] H.E. Hoefdraad, The charge-transfer absorption band of Eu^{3+} in oxides, J. Solid State Chem. 15 (1975) 175–177.

[69] K. E, C.K. Jørgensen: Modern Aspects of Ligand Field Theory. North-Holland Publishing Co. 1971. VIII, p. 538, Preis: Hfl. 100.–, Berichte der Bunsengesellschaft für physikalische Chemie, 75, 10, 1971, pp.1150–1150.

[70] S.K. Gupta, M. Mohapatra, V. Natarajan, S.V. Godbole, Site-specific luminescence of Eu^{3+} in gel-combustion-derived strontium zirconate perovskite nanophosphors, J. Mater. Sci. 47 (2012) 3504–3515.

[71] G.S. K, B.M. Krishnadas, G.S. Vasant, N. Venkataraman, Probing site symmetry around Eu^{3+} in nanocrystalline ThO_2 using time resolved emission spectroscopy, J. Am. Ceram. Soc. 97 (2014) 3694–3701.

[72] K. Binnemans, Interpretation of europium(III) spectra, Coord. Chem. Rev. 295 (2015) 1–45.

[73] Q. Ju, Y. Liu, R. Li, L. Liu, W. Luo, X. Chen, Optical spectroscopy of Eu^{3+}-doped BaFCl nanocrystals, J. Phys. Chem. C 113 (2009) 2309–2315.

[74] M.A. Ahmed, E. Ateia, F.M. Salem, The effect of Ti^{4+} ions and gamma radiation on the structure and electrical properties of Mg ferrite, J. Mater. Sci. 42 (2007) 3651–3660.

[75] A.V. Raut, D.V. Kurmude, D.R. Shengule, K.M. Jadhav, Effect of gamma irradiation on the structural and magnetic properties of Co–Zn spinel ferrite nanoparticles, Mater. Res. Bull. 63 (2015) 123–128.

[76] Y. Eagleman, M. Weber, S. Derenzo, Luminescence study of oxygen vacancies in lanthanum hafnium oxide, $La_2Hf_2O_7$, J. Lumin. 137 (2013) 93–97.

[77] S.K. Gupta, P. Ghosh, C. Reghukumar, N. Pathak, R. Kadam, Experimental and theoretical approach to account for green luminescence from $Gd_2Zr_2O_7$ pyrochlore: exploring the site occupancy and origin of host-dopant energy transfer in $Gd_2Zr_2O_7$:Eu^{3+}, RSC Adv. 6 (2016) 44908–44920.

[78] S.K. Gupta, P. Ghosh, K. Sudarshan, R. Gupta, P. Pujari, R. Kadam, Multifunctional pure and Eu^{3+} doped β-Ag_2MoO_4: photoluminescence, energy transfer dynamics and defect induced properties, Dalton Trans. 44 (2015) 19097–19110.

[79] S.K. Gupta, P.S. Ghosh, A.K. Yadav, S.N. Jha, D. Bhattacharyya, R.M. Kadam, Origin of blue-green emission in α-$Zn_2P_2O_7$ and local structure of Ln^{3+} Ion in α-$Zn_2P_2O_7$:Ln (Ln = Sm, Eu): time-resolved photoluminescence, EXAFS, and DFT measurements, Inorg. Chem. 56 (2016) 167–178.

[80] S.K. Gupta, M. Mohapatra, S. Godbole, V. Natarajan, On the unusual photoluminescence of Eu^{3+} in α-$Zn_2P_2O_7$: a time resolved emission spectrometric and Judd–Ofelt study, RSC Adv. 3 (2013) 20046–20053.

[81] S.K. Gupta, B. Rajeshwari, S. Achary, S. Patwe, A. Tyagi, V. Natarajan, R. Kadam, Europium luminescence as a structural probe: structure-dependent changes in Eu^{3+}-substituted $Th(C_2O_4)_2{\cdot}xH_2O$ (x = 6, 2, and 0), Eur. J. Inorg. Chem. 2015 (2015) 4429–4436.

[82] S.K. Gupta, K. Sudarshan, P. Ghosh, K. Sanyal, A. Srivastava, A. Arya, P. Pujari, R. Kadam, Luminescence of undoped and Eu^{3+} doped nanocrystalline $SrWO_4$ scheelite: time resolved fluorescence complimented by DFT and positron annihilation spectroscopic studies, RSC Adv. 6 (2016) 3792–3805.